LUND UNIVERSITY

Assessment of mobile radiometry data in radiological emergencies using Bayesian statistical methods

Bukartas, Antanas

2021

Document Version:
Publisher's PDF, also known as Version of record

Link to publication

Citation for published version (APA):
Bukartas, A. (2021). *Assessment of mobile radiometry data in radiological emergencies using Bayesian statistical methods*. Lund University, Faculty of Medicine.

Total number of authors:
1

General rights
Unless other specific re-use rights are stated the following general rights apply:
Copyright and moral rights for the publications made accessible in the public portal are retained by the authors and/or other copyright owners and it is a condition of accessing publications that users recognise and abide by the legal requirements associated with these rights.
• Users may download and print one copy of any publication from the public portal for the purpose of private study or research.
• You may not further distribute the material or use it for any profit-making activity or commercial gain
• You may freely distribute the URL identifying the publication in the public portal

Read more about Creative commons licenses: https://creativecommons.org/licenses/

Take down policy
If you believe that this document breaches copyright please contact us providing details, and we will remove access to the work immediately and investigate your claim.

LUND UNIVERSITY

PO Box 117
221 00 Lund
+46 46-222 00 00

Assessment of mobile radiometry data in radiological emergencies using Bayesian statistical methods

ANTANAS BUKARTAS
MEDICAL RADIATION PHYSICS, MALMÖ | FACULTY OF MEDICINE | LUND UNIVERSITY

Printed by Media-Tryck, Lund 2021 NORDIC SWAN ECOLABEL 3041 0903

LUND UNIVERSITY

FACULTY OF MEDICINE

Department of Translational Medicine
Medical Radiation Physics, Malmö

Lund University, Faculty of Medicine
Doctoral Dissertation Series 2021:90
ISBN 978-91-8021-097-3
ISSN 1652-8220

Assessment of mobile radiometry data in radiological emergencies using Bayesian statistical methods

Assessment of mobile radiometry data in radiological emergencies using Bayesian statistical methods

Antanas Bukartas

Supervisors:

Christopher Rääf, Robert Finck and Jonas Wallin

LUND
UNIVERSITY

DOCTORAL DISSERTATION

by due permission of the Faculty of Medicine, Lund University, Sweden.
To be defended at Medelhavet, Wallenberg building, S. Förstadsgatan 101, 21401 Malmö, Skåne University Hopsital SUS Malmö.

2021-09-17, 09:00 CET.

Faculty opponent:
Dr. Tzany Kokalova Wheldon, University of Birmingham

Organization LUND UNIVERSITY Medical Radiation Physics, Malmö Carl-Bertil Laurells gata 9, 20502, Malmö	**Document name** DOCTORAL DISSERTATION **Date of disputation** 2021-09-17
Author(s) Antanas Bukartas	**Sponsoring organization** Strålsäkerhetsmyndigheten

Title and subtitle

Assessment of mobile radiometry data in radiological emergencies using Bayesian statistical methods

Abstract

Nuclear technology and the use of radiation sources have been extensively adopted in the modern world. Despite that, a number of radiological accidents, significantly affecting population and the environment, has happened. Few of the most known are accidents in Chernobyl and Fukushima nuclear power plants. As a result, significant areas are still contaminated with some residential areas evacuated. To estimate the possibility to return to an affected area, the spatial distribution of deposition density of the radionuclides within the area has to be evaluated using mobile gamma spectrometry. In radiological emergencies involving lost radioactive sources, mobile gamma spectrometry equipment is used to survey the area where the source is suspected to be, trying to localize and identify the radioactive source. For both: radionuclide spatial distribution estimation and localization of a source problems, the most prominent methods of data analysis were established decades ago and are robust and easy to utilise. Despite that, the usual methods, like interpolation or setting an alarm threshold level, do not use all of the available data in the measurement time-series to produce an estimation of the situation.

Using Bayesian statistics it is possible to combine the prior knowledge about the situation with the data, to obtain predictions about the situation. Thus, the aim of this thesis was to investigate the feasibility of a Bayesian-based approach for mobile gamma spectrometry applications in radiological emergencies. A Bayesian algorithm was developed for analysing measurement time-series to extract the physical location and source strength in an orphan source search and to map radionuclide deposition in an area of interest. It was found that the Bayesian methods could be successfully applied to obtain the predicted position and activity of the source or the spatial deposition of the radionuclide within an area. It was also found that the accuracy of the Bayesian estimations is heavily dependent on the quality and quantity of the data, the more and the better quality data – the better the assessments. A comparison of the most prominent method for an orphan source detection using alarm threshold levels with the Bayesian method, in terms of detection probability of orphan sources using simulated data, has shown that the Bayesian algorithm can potentially detect the radioactive sources more reliably than the usual alarm threshold method due to the inclusion of all of the data in the measurement time-series.

The overall conclusion of the thesis is that Bayesian methods can be successfully applied to mobile spectrometry data. The mapping and positioning of gamma emitting radionuclides can be done more precisely and provide more information about the radiation in the environment during radiological accident scenarios. Despite the shown potential of Bayesian methods in mobile gamma spectrometry within this thesis, further investigations are needed to validate the findings discussed.

Key words

Mobile gamma spectrometry, gamma, spectrometry, orphan source, lost source, ionizing radiation, Bayesian, activity, position, activity density, reconstruction, UAV, car-borne

Classification system and/or index terms (if any)

Supplementary bibliographical information		**Language** English
ISSN: 1652-8220		**ISBN: 978-91-8021-097-3**
Recipient's notes	**Number of pages** 188	Price
	Security classification	

I, the undersigned, being the copyright owner of the abstract of the above-mentioned dissertation, hereby grant to all reference sources permission to publish and disseminate the abstract of the above-mentioned dissertation.

Signature  Date: 2021-08-12

Assessment of mobile radiometry data in radiological emergencies using Bayesian statistical methods

Antanas Bukartas

LUND
UNIVERSITY

Front cover by Antanas Bukartas

Aerial photo of the mobile gamma spectrometry vehicle used in the thesis during angular efficiency calibration of the detectors.

Copyright pp 1-90 Antanas Bukartas

Paper 1 © 2018 by the Authors, (published open access by Elsevier Ltd. under the licence CC BY-NC-ND 4.0)

Paper 2 © 2021 by the Authors (Published open access by PLOS ONE under CC BY 4.0)

Paper 3 © 2021 by the Authors (Accepted for publishing in PLOS ONE with major revisions)

Paper 4 © by the Authors (To be submitted for publishing in Radiation Measurements)

Paper 5 © by the Authors (Manuscript)

Faculty of Medicine
Department of Translational Medicine

ISBN 978-91-8021-097-3
ISSN 1652-8220

Printed in Sweden by Media-Tryck, Lund University
Lund 2021

Media-Tryck is a Nordic Swan Ecolabel certified provider of printed material. Read more about our environmental work at www.mediatryck.lu.se

MADE IN SWEDEN

To my family

Table of Contents

Abstract

Nuclear technology and the use of radiation sources have been extensively adopted in the modern world. Despite that, a number of radiological accidents, significantly affecting population and the environment, has happened. Few of the most known are accidents in Chernobyl and Fukushima nuclear power plants. As a result, significant areas are still contaminated with some residential areas evacuated. To estimate the possibility to return to an affected area, the spatial distribution of deposition density of the radionuclides within the area has to be evaluated using mobile gamma spectrometry. In radiological emergencies involving lost radioactive sources, mobile gamma spectrometry equipment is used to survey the area where the source is suspected to be, trying to localize and identify the radioactive source. For both: radionuclide spatial distribution estimation and source localization problems, the most prominent methods of data analysis were established decades ago and are robust and easy to utilise. Despite that, the usual methods, like interpolation or using an alarm threshold level, do not use all of the available data in the measurement time-series to produce an estimation of the situation.

Using Bayesian statistics it is possible to combine the prior knowledge about the situation with the data, to obtain predictions about the situation. Thus, the aim of this thesis was to investigate the feasibility of a Bayesian-based approach for mobile gamma spectrometry applications in radiological emergencies. A Bayesian algorithm was developed for analysing measurement time-series to extract the physical location and source strength in an orphan source search and to map radionuclide deposition in an area of interest. It was found that the Bayesian methods could be successfully applied to obtain the predicted position and activity of the source or the spatial deposition of the radionuclide within an area. It was also found that the accuracy of the Bayesian estimations is heavily dependent on the quality and quantity of the data, the more and the better quality data – the better the assessments. A comparison of the most prominent method for an orphan source detection using alarm threshold levels with the Bayesian method, in terms of detection probability of orphan sources using simulated data, has shown that the Bayesian algorithm can potentially detect the radioactive sources more reliably than the usual alarm threshold method due to the inclusion of all of the data in the measurement time-series.

The overall conclusion of the thesis is that Bayesian methods can be successfully applied to mobile spectrometry data. The mapping and positioning of gamma emitting radionuclides can be done more precisely and provide more information about the radiation in the environment during radiological accident scenarios. Despite the shown potential of Bayesian methods in mobile gamma spectrometry within this thesis, further investigations are needed to validate the findings discussed.

Popular Scientific Summary

Radioactivity for many is a frightening word. Even though in 2020 there were around 500 operational nuclear reactors throughout the world with more being built and millions of radioactive sources being used in industry, agriculture and medicine, radioactivity will for many always be associated with the history of Chernobyl, Fukushima accidents alongside the horrors of Hiroshima and Nagasaki. In some sense, these fears may be warranted. In the hands of unaware persons, radioactive sources can become lethal, especially for those unaware of how ionising radiation can cause biological effects when in near contact with a radioactive object. Experience has shown that warning signs can be blatantly ignored, and that peculiar features of highly radioactive sources, such as phosphorescence of CsCl powder, can be misconceived as amazing curiosity objects, causing inadvertent exposure of even more persons. These examples are snapshots of real accidents, where several people died due to excess exposures to radioactive sources which were lost or abandoned. It is furthermore possible that such sources might be dispersed on purpose as a malevolent act of perpetrators or left behind due to plain negligence of people handling the sources, but many times it is just an unexpected accident.

Furthermore, accidental releases from nuclear facilities can cause widespread dispersion of radioactive fallout over rural and urban areas, where long-lived gamma emitting radionuclides will cause excess exposure of humans. In such situations protecting public and the environment is of greatest priority. Fast and efficient methods of either localising a lost radioactive source or obtaining a radioactivity map of a contaminated residential area is therefore key to correctly evaluate the emergency situation and deal with it an appropriate manner.

Measurement methods to locate and determine the magnitude of the radioactive sources are well known and have been established decades ago. One of these methods include using mobile units equipped with gamma radiation sensitive detectors that are used to search areas to locate lost sources. This technique is usually referred to as mobile radiometry or mobile spectrometry and has proven to work relatively fast and reliably, warranting their use in radiological emergency situations. Despite that, not all information within these mobile measurements is used to draw the full conclusions about the situation.

Bayesian statistics is an old statistical data analysis toolset which saw a modern revival due to outstanding increases in computational power of modern computers.

It allows to combine prior information about the situation with data to obtain predictions about the situation.

In this thesis, Bayesian statistical data analysis methods were used to develop and test a set of algorithms. The first one presented here estimates the position and activity of a lost radioactive source from the measurements made by mobile detectors, while passing a gamma radiation source at certain distances. The second algorithm can be used to map a surface deposition of fallout of gamma emitting radionuclides within a limited area.

The overall conclusion of the thesis is that Bayesian methods can successfully be applied to mobile spectrometry data, so that positioning and mapping of gamma emitting radionuclides can be done more precisely and provide more information about the radiation environment in radiological accident scenarios. Despite that, further investigations should be performed in the applicability and validity of the method to fully exploit the potential of the Bayesian methods.

Original Articles

This thesis is based on the following papers, which will be referred to in the text by their Roman numerals.

I. "A Bayesian method to localize lost gamma sources", **A. Bukartas,** R. Finck, J. Wallin, C. L. Rääf, Applied Radiation and Isotopes, Volume 145, March 2019, Pages 142-147

II. "Bayesian algorithm to estimate position and activity of an orphan gamma source utilizing multiple detectors in a mobile gamma spectrometry system", **A. Bukartas,** J. Wallin, R. Finck, C. Rääf, PLOS ONE 16(1) Date of publication: 22 January 2021.

III. "Accuracy of a Bayesian technique to estimate position and activity of orphan gamma-ray sources by mobile gamma spectrometry: Influence of imprecisions in positioning systems and computational approximations", **A. Bukartas**, J. Wallin, R. Finck, C. Rääf, Manuscript accepted with major revisions in PLOS ONE

IV. "Maximum detection distances for gamma emitting point sources in mobile gamma spectrometry", R. Finck, **A. Bukartas**, M. Jönsson, C. Rääf, Manuscript to be submitted to Radiation Measurements

V. "Applicability of a Bayesian method for reconstruction of ground activity deposition based on synthetic airborne gamma spectrometric data", **A. Bukartas**, R. Finck, J. Wallin, C. Rääf, Manuscript

Abbreviations

AGS – Airborne Gamma Spectrometry

GNSS – Global Navigation Satellite System

HPGe – High Purity Germanium

LIDAR – Light Detection and Ranging

MCA – Multichannel Analyser

MCMC – Markov Chain Monte-Carlo

MDD – Maximal Detection Distance

MH – Metropolis-Hastings

NaI(Tl) – Sodium Iodide doped with Thallium

PKI – Point-Kernel Integration

ROI – Region of Interest

SNR – Signal-to-Noise Ratio

UAV – Unmanned Aerial Vehicle

Introduction and objectives

Nuclear technology and use of radiation sources have been extensively adopted in the modern world, ranging from the energy industry to widely known applications in medical physics. Despite the rigorous safety rules developed, radiological accidents still happen and have, in some situations, previously affected the population significantly, with the most notable examples being accidents in the Fukushima and Chernobyl nuclear power plants [1], [2]. During a severe accident in a nuclear power plant of such scale, significant areas can be contaminated by the fallout of atmospherically dispersed radionuclides. As a result, significant portions of the population in highly contaminated residential areas might need to be relocated to avoid the adverse effects of ionising radiation. The spatial distribution of deposited radionuclides has to be evaluated to possibly decide on remediation actions to be able to return to the area [3].

The use of radioactive sources is governed by rigorous safety rules to avoid accidents, theft or intentional malicious use [4]. Nevertheless, sources can be misplaced or lost out of regulatory control [5]–[7]. One example of such an accident was in Goiania, Brazil when a ^{137}Cs teletherapy source was left behind when a private radiotherapy clinic moved to new premises and did not inform the regulatory bodies accordingly [6]. During the demolition of the hospital premises, two persons looking for scrap metal found the source. Not knowing what it was, they took it home and tried to open it, assuming it could have some scrap value. Consequently, four persons died, 249 persons were contaminated, 42 buildings were decontaminated, and five buildings were demolished. It was necessary to remove 3500 m^3 of radioactive waste from the premises of the village. In 2001 another similar incident happened in Georgia, when three persons collecting firewood found two lost and unmarked ^{90}Sr sources, which they used as heaters throughout the cold winter night. One person died due to the received radiation dose [5].

Another potential radiological threat is during launch or re-entry into the atmosphere of space vehicles carrying nuclear reactors or radioisotope thermoelectric generators, which in some missions are used to produce electric power in space. On 11-th of July, 1970, as a part of a routine testing program, the U.S. Air Force launched an Athena missile from Green River, Utah. There were two ^{57}Co sources of approximately 17.4 GBq each in the nose cone of the missile. The missile malfunctioned resulting in an impact in Mexico [8]. In 1978, control of

satellite Kosmos 954 was lost, resulting in erratic changes of the orbit due to malfunctioning control systems. Later, the satellite re-entered the atmosphere and was torn into many pieces. The debris was deposited in Canadian territory along a 600 km path. An extensive effort called “Operation Morning Light” was initiated to recover as much of the radioactive material as possible to avoid harm to the public [9], [10].

Regardless of the particularities of the radiological accident, the main challenge is to obtain as much information about the situation as possible in the shortest amount of time, utilising the least resources possible to provide the necessary information for the decision-makers managing the radiological accident. Relatively simple and robust data analysis methods established decades ago using mobile gamma spectrometry are prevalent in such circumstances where there is a significant possibility for the lack of time, equipment and staff [11]. Despite the straightforwardness of the well-established methods, they do not utilise all of the information present in the obtained measurement time-series of the mobile gamma spectrometry systems. By using, e.g. Bayesian methods for combining measured data with the physical laws of radiation transport, it is possible to obtain more exhaustive information of a radiation situation [12]–[17]. In mobile searching for lost gamma-ray sources, conventional methods can indicate the presence of a source, but Bayesian methods will also have the potential to provide information of its activity and distance from the detection equipment, as shown in this work.

Thus, the specific aim of this thesis was to investigate the feasibility of a Bayesian-based approach for mobile gamma spectrometry applications in radiological emergencies, by developing a Bayesian algorithm for analysing measurement series to extract the physical location and source strength in orphan source search and mapping of radionuclide deposition in an area of interest.

Theory

Bayesian inference

In most of this thesis, Bayesian methods are applied to perform Bayesian inference and obtain helpful information in orphan source search missions or reconstruction of the distribution of radionuclide deposition. Bayesian inference is a statistical method employing the Bayes theorem for combining prior knowledge with new information, resulting in posterior probability distributions of the parameters of interest [18]. The basis for the formulation of the Bayesian equation stems from the formulation of conditional probability. It is well-known that the conditional probability, $p(A|B)$, can be expressed as:

$$p(A|B)=\frac{p(A\cap B)}{p(B)}. \qquad 1$$

Because $p(A\cap B)=p(B\cap A)$, it is possible to obtain an expression:

$$p(A|B)=\frac{p(B|A)p(A)}{p(B)}. \qquad 2$$

This equation is called the Bayesian equation and is the cornerstone of the Bayesian inference utilised in papers I-III and V presented in this thesis. Because it may be difficult to calculate, $p(B)$, in practice, and that, $p(B)$, only functions as a normalising factor, the posterior distribution $p(A|B)$ is usually evaluated using expression:

$$p(A|B)\propto p(B|A)p(A), \qquad 3$$

where $p(A)$ is the prior and $p(B|A)$ is the likelihood. The sign $\propto$ in the Eq. 3, denotes proportionality up to a normalising constant.

Thus, to perform the Bayesian inference, a Bayesian model must be constructed, comprising of two constituents: a prior and a likelihood. Before performing the

measurements, the available information constitutes the prior, describing the knowledge about the parameters of interest by assigning them selected probability distributions. The likelihood describes how well the data is supported by the chosen model and selected values of parameters of interest. An example of a Bayesian calculation for an arbitrary parameter of interest is displayed in Fig. 1.

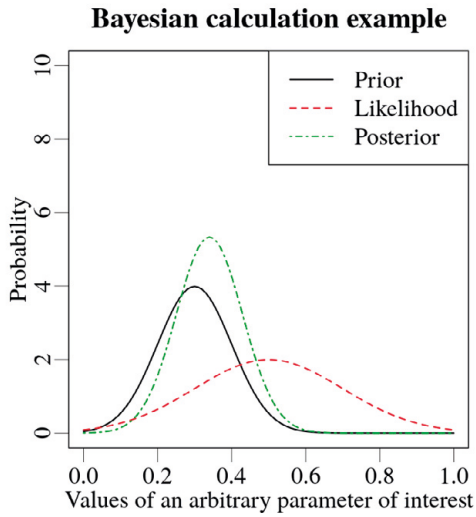

Fig. 1. An example of a Bayesian calculation. A prior distribution is displayed as the black curve, the likelihood is represented by the red dashed curve and the product of those two distributions, denoted the posterior distribution, is given by the green dot-dashed curve. The posterior can be updated again using new knowledge.

Further in this work, after introducing the physics of gamma-ray transport and interaction in matter required to formulate the Bayesian models, two specific Bayesian models will be built for two different purposes. One that localises and estimates the activity of gamma-ray point source from mobile gamma spectrometry data collected along a road and another that reconstructs the spatial distribution of radionuclide distribution of an area of interest on the ground from aerial gamma spectrometry data.

Performing Bayesian inference on position and activity of an unshielded gamma-ray point source

Count-rate in a radiation detector

Let us consider an unshielded, gamma-ray point source of activity A positioned at a distance d from a road (Fig. 2). The primary photon fluence rate (expressed in units of $s^{-1}m^{-2}$) at any position along the road with the distance r to the radioactive source (Fig. 2) during an acquisition time interval can be expressed as:

$$\dot{\varphi}(r) = \frac{A n_\gamma e^{-\mu_{air} r}}{4\pi r^2}, \qquad 4$$

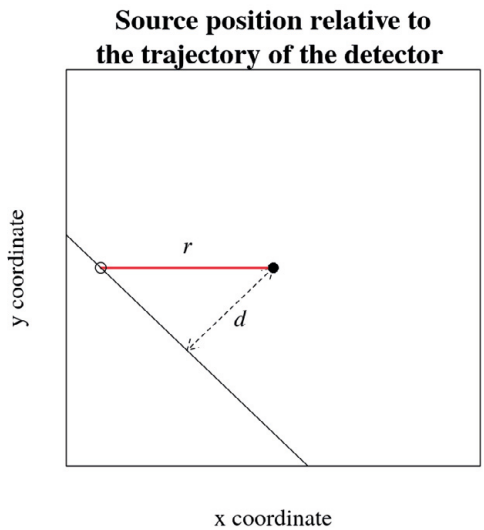

Fig. 2. An illustration of the position of the source (black dot) relative to the trajectory of the detector (black line). The distance between the source and the trajectory of the detector d is displayed by a dotted arrow. The source-detector distance r for a chosen point (black circle) along the trajectory of the detector is marked by a thick red line.

where n_γ is the branching ratio for the particular photon energy, E_γ, of the radionuclide in the source, denoting the number of photons of energy E_γ emitted per decay, μ_{air} is the linear photon attenuation coefficient in air for photon energy E_γ. It has to be noted that the linear photon attenuation coefficient μ_{air} is calculated from the mass attenuation coefficient $\mu_{air,mass}$ and the density of the attenuating material (in this case air) ρ_{air}, yielding $\mu_{air} = \mu_{air,mass} \cdot \rho_{air}$ [19].

The counting efficiency of the detector has to be determined to convert between measured detector count-rate $\dot{N}$ and photon fluence rate $\dot{\varphi}$. The counting efficiency

depends on i) the geometric efficiency $\varepsilon_{\text{geom}}$, which is the ratio between the total number of emitted photons to the number of photons arriving at the detector, and ii) the intrinsic efficiency $\varepsilon_{\text{intr}}$, which is the ratio between the number of photons arriving at the detector and the number of photons detected in the detector:

$$\varepsilon = \varepsilon_{\text{geom}} \cdot \varepsilon_{\text{intr}}. \qquad 5$$

The geometric efficiency of the detector depends on the distance between the radioactive source and the detector. The farther the source is from the detector, the smaller the solid angle subtended by the detector from the perspective of the radioactive source, and hence the smaller the geometric efficiency leading to a lower number of photons impinging at the detector. Because the typical source-detector distances, *r,* in orphan source search scenarios are much larger than the dimensions of the active medium of the detectors, the incoming photons can be regarded as parallel.

For an ideal detector the intrinsic efficiency does not depend on the geometrical configuration, thus utilising parallel photon approximation counting efficiency of a radiation detector, ε, can instead be expressed as a ratio between the count-rate in the detector, $\dot{N}$, and the fluence rate of photons at the detector, $\dot{\varphi}$. The counting efficiency of a detector can, expressed in this way, be regarded as a virtual "effective detector area":

$$\varepsilon(E_\gamma) = \frac{\dot{N}(E_\gamma)}{\dot{\varphi}(E_\gamma)}, \qquad 6$$

where $\dot{N}(E_\gamma)$ is the count-rate in a spectral energy window (or Region-of-Interest, ROI) centred around energy E_γ, and $\dot{\varphi}(E_\gamma)$is the fluence rate at the detector of photons of energy E_γ. Then, if the detector is stationary relative to the unshielded gamma-ray point source, emitting a number An_γ photons of energy E_γ isotropically, the expected count-rate value, $\dot{N}_{\text{source}}$, will be constant and proportional to the counting efficiency of the detector ε throughout the measurement:

$$\dot{N}_{\text{source}}(r, E_\gamma) = \frac{A n_\gamma \varepsilon(E_\gamma) e^{-\mu_{\text{air}}(E_\gamma) r}}{4\pi r^2}. \qquad 7$$

Considering a stationary measurement at a distance r from the radioactive source, the average value of the count-rate due to background radiation will be constant. Thus, the total number of counts in the detector $\dot{N}_{\text{sum}}$ can be calculated as a linear combination of the average count-rate due to the presence of the source $\dot{N}_{\text{source}}$, and the average background count-rate in the spectral window of the primary photons, c:

$$\dot{N}_{\text{sum}} = \dot{N}_{\text{source}} + c. \qquad 8$$

The complete equation, describing the count-rate in a detector for a stationary measurement in an environment with a constant background radiation can then be written as:

$$\dot{N}_{\text{sum}}(r, E_\gamma) = \frac{A n_\gamma \varepsilon e^{-\mu_{\text{air}} r}}{4\pi r^2} + c. \qquad 9$$

Peak in the count-rate function

In a situation, where a detector moves in a straight line at a constant velocity v past a radioactive source positioned at a distance d from the detector's trajectory (Fig. 2), the detector's count-rate will change while passing the source. Starting at a distance r very far away from the radioactive source, the r^2 term and the exponential $e^{-\mu_{\text{air}} r}$ terms in the count-rate function (Eq. 9) will yield infinitesimally small count-rate values regardless of the source activity. While the distance between the detector and the source r is decreasing, the count-rate will increase until the shortest source-detector distance r_{min} is reached, which is equal to the distance from the source to the trajectory of the detector $r_{\text{min}}=d$. At this point, the count-rate will be the highest, as illustrated in Fig. 3. Continuing along the straight trajectory past the radioactive source will increase the source-detector distance r and decrease the count-rate, $\dot{N}_{\text{sum}}$, in the detector. The varying count-rate while passing a radioactive source will form a visible peak as illustrated in Fig. 3, provided that the number of photons emitted by the source is sufficient and it is close enough to the mobile detector pathway. In essence, such a count-rate function displays the average count-rate values for many one-second stationary measurements with infinitesimally small distances between the measurement points. A change in the number of photons emitted by the source An_γ, will change the height of the peak in the count-rate function. A change in the position of the source, resulting in a different distance from the source to the trajectory of the detector, d, will alter both the width and height of the peak.

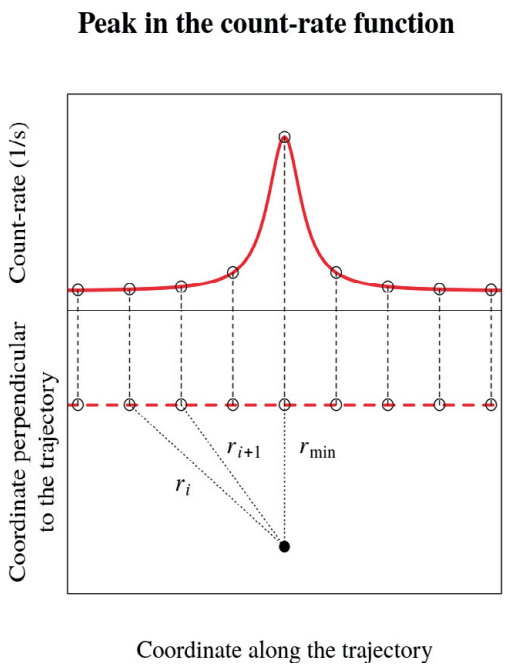

Fig. 3. An illustration of the arising peak in the count-rate function (top) due to changing source-detector distance r while passing a source (bottom). The source is marked with a black dot, and the trajectory of the detector – red dashed line (bottom). Some values in the count-rate function graph are marked with black circles. The corresponding positions at which these values were evaluated are marked on the trajectory in the same way, and connected with vertical dashed lines across the count-rate (top) and geographical coordinate (bottom) graph boundary. Distance to one of the points is marked r_i, and the adjacent one – r_{i+1}. Passing the minimal source-detector distance $r_{\min}$, which is equal to the distance from the source to the trajectory of the detector d, yields the highest count-rate.

In most cases, during orphan source search missions the radiation detection system is configured to provide counts integrated over a specific acquisition time [20]–[23]. During that acquisition time interval, the detector and source can be varyingly aligned. Therefore, the maximum count-rate value can occur anywhere within an acquisition interval. Fig. 4 illustrates two extremes of such relative alignment with the maximum count-rate function in the centre and at the edge of the interval.

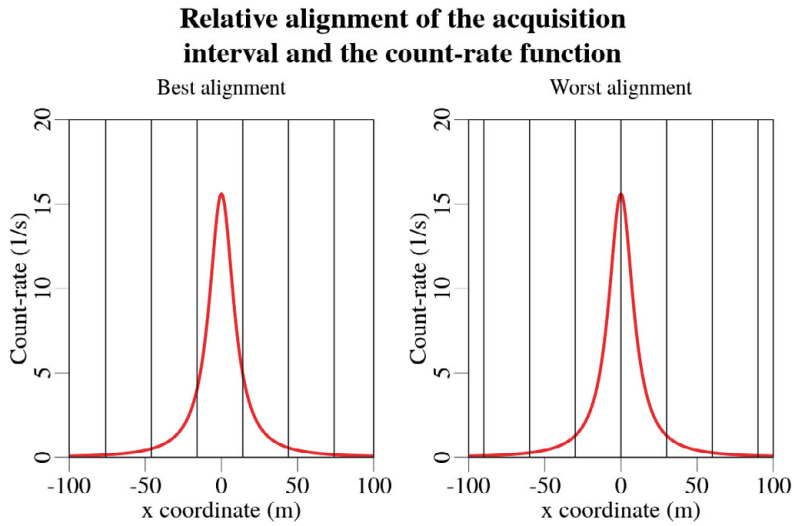

Fig. 4. Relative alignment of the acquisition time slots to the count-rate function. Borders between adjacent acquisition time slots is marked by vertical lines. Theoretically, the graph on the left denotes the best alignment resulting in the highest count-rate in a single acquisition time slot. The graph on the right illustrates the worst alignment when the portion of the peak in the measurement time-series with the highest number of counts is divided between two adjacent measurement time-slots.

Different relative alignments will thus result in different maximum attainable counts within an acquisition time interval during a passage of the radioactive source. In the best-alignment situation, the maximum attainable counts in an acquisition time interval at the shortest source-detector distance will be the highest. In the worst alignment situation, the maximum attainable counts will be the lowest. However, the total number of counts for the entire passage of the source will be the same for best and worst alignments. The misalignment illustrated in Fig. 4 will depend on the distance to the source and the length of the acquisition time interval.

Angular variations in counting efficiency

The detector's medium in a gamma spectrometer is always surrounded by material that, to some extent, shields and scatters photons. It can be a cooling dewar for an HPGe detector, photomultiplier tube with electronics for a NaI(Tl) detector, or even some vehicle's structural components, inside which the detector system is mounted. Probably there will be different amounts of shielding between the source and the detector's medium for different angles of incidence as a detector is moving past a radioactive source. Thus, the counting efficiency of the detector will depend on the photon angle of incidence. These angular efficiency variations can be expressed as a relative detector efficiency, ε_{rel}, which is a dimensionless

number, that multiplied by the counting efficiency for the reference direction, $\varepsilon_{\mathrm{ref}}$, gives the counting efficiency for any other selected incident direction θ:

$$\varepsilon(E_\gamma, \theta) = \varepsilon_{\mathrm{rel}}(E_\gamma, \theta)\,\varepsilon_{\mathrm{ref}}(E_\gamma). \qquad 10$$

The expression for the incident direction θ of the photon fluence must be formulated to obtain the angular efficiency correction for the analytical expression of the count-rate function. It is possible to do so using a difference between two-parameter arctangent functions calculated for the vehicle velocity, $\boldsymbol{v}$, and detector-to-source, $\boldsymbol{r}$, vectors. The velocity vector is evaluated from the geographical coordinates in two spatial dimensions retrieved from a global navigation satellite system (GNSS) receiver at a set rate while the detector was moving past the source:

$$X = x_1, x_2, \ldots, x_i, \ldots, x_n \qquad 11$$

where x_i is the i-th measured coordinate in two dimensions (x' is the x geographical coordinate and x'' is the y geographical coordinate). The velocity vector $\boldsymbol{v}_i$ of the i-th measurement can then be expressed as a difference between the current (i) and previous (i-1) geographical coordinates in two spatial dimensions:

$$\boldsymbol{v_i} = \begin{bmatrix} v_i' \\ v_i'' \end{bmatrix} = \begin{bmatrix} x'_i - x'_{i-1} \\ x''_i - x''_{i-1} \end{bmatrix}. \qquad 12$$

Then, for an arbitrary position of the source $\boldsymbol{p}$, we can estimate a detector-to-source vector $\boldsymbol{r}$:

$$\boldsymbol{r_i} = \begin{bmatrix} r_i' \\ r_i'' \end{bmatrix} = \begin{bmatrix} x'_i - p' \\ x''_i - p'' \end{bmatrix}, \qquad 13$$

where p' is the first and p'' is the second spatial coordinate of the source position $\boldsymbol{p}$. It is then possible to calculate the angle of incidence for any combination of measurement coordinate x_i and chosen source position $\boldsymbol{p}$ by subtracting the values yielded by a two-parameter arctangent function for the detector-to-source vector $\boldsymbol{r_i}$ from a two-parameter arctangent function for the velocity vector $\boldsymbol{v_i}$ for the measurement i:

$$\theta_i(\boldsymbol{v_i}, \boldsymbol{r_i}) = \mathrm{atan2}(v_i'', v_i') - \mathrm{atan2}(r_i'', r_i'), \qquad 14$$

where the v' and r' denote the first spatial coordinate and v'' and r'' – the second spatial coordinate of the respective vectors. Here, the relative angle of incidence θ

can obtain values $\theta \in [0;360)$ degrees. Angle of 0 degrees is the driving direction of the vehicle. Because this angle of incidence, θ, in principle only depends on the position of the source $\boldsymbol{p}$, the current measurement position x_i and the previous measurement position x_{i-1}, it is possible to redefine the previous equation by denoting the difference in two-parameter arctangent functions as a function f_{angle}:

$$f_{\text{angle},i}(\boldsymbol{p}, x_i, x_{i-1}) = \theta(\boldsymbol{v_i}, \boldsymbol{r_i}) = \theta\left(\begin{bmatrix} x'_i - x'_{i-1} \\ x''_i - x''_{i-1} \end{bmatrix}, \begin{bmatrix} x'_i - p' \\ x''_i - p'' \end{bmatrix}\right). \quad 15$$

Then, using this function, count-rate in the detector (Eq. 9) with angular variations in the counting efficiency can be expressed for an angle of incidence resulting from any two subsequent measurement coordinates, $x_i, x_{i-1} \in X$, and source position $\boldsymbol{p}$:

$$\dot{N}_{\text{sum},i}(\boldsymbol{p}, x_i, x_{i-1}, E_\gamma) = \frac{A n_\gamma \varepsilon_{\text{ref}}(E_\gamma) \varepsilon_{\text{rel}}(E_\gamma, f_{\text{angle}}(p, x_i, x_{i-1})) e^{-\mu_{\text{air}} \| x_i - p \|}}{4\pi \| x_i - p \|^2} + c. \quad 16$$

Returning to the discussions about the shape of the peak in the count-rate function from the previous section, it is now evident how the geometrical configuration of the sensitive medium of the detector, the way the radiation detector is mounted, the additional shielding provided by the vehicle surrounding the detector will alter the shape of the peak in the count-rate function. As additional shielding in any direction will only decrease the number of detected photons, it is desirable to mount the detector in a way which minimises this shielding effect. A coaxial HPGe detector can, for example, be installed in the vehicle with the crystal facing upwards and the dewar downwards.

Point-kernel approximation of mobile measurements

When a gamma spectrometer is moving past an unshielded gamma-ray point source in a straight trajectory, the number of counts acquired during an acquisition time interval, t_{acq}, will depend on the length of the interval, the detector's speed, the angle of incidence and the distance between the source and the trajectory of the detector. The longer the acquisition time interval, the lower the speed and the closer the distance between the source and the detector, the more counts are acquired. An illustration of acquisition time interval, t_{acq}, during a passage of a source is displayed in Fig. 5, with the green area representing the acquired number of counts.

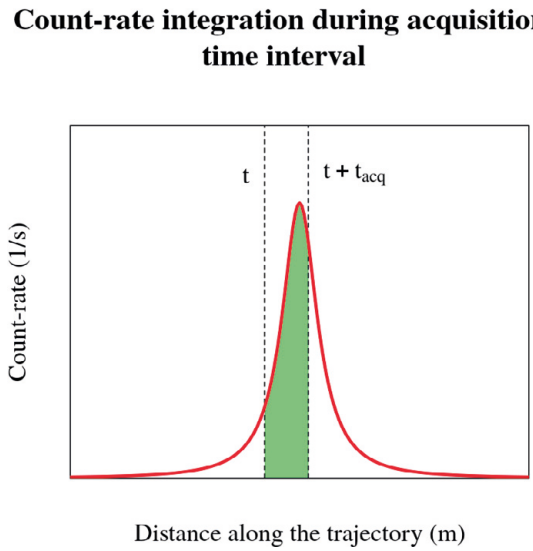

Fig. 5. An illustration of the integration of the count-rate function during an acquisition time interval. The vertical dashed lines mark the beginning and the end of the interval. The shaded green area under the count-rate function and between the vertical dashed lines is the integrated area of the count-rate function.

These counts represent an average of the count-rate function during the acquisition time interval. For simplicity, assuming an ideal detector with no angular variations in counting efficiency, the count-rate during an acquisition time interval would become:

$$\dot{N}(t) = \int_{t}^{t+t_{\mathrm{acq}}} \frac{A\, n_{\gamma}\, \varepsilon\, e^{-\mu_{\mathrm{air}} r(t)}}{4\pi r(t)^2}\, dt. \qquad 17$$

In a typical orphan source search scenario using car-borne gamma spectrometry, the usual speed of the vehicle would be about 50 km/h combined with acquisition time intervals of 1 s [11], [24], [25]. In such circumstances, a slight difference in the expected number of counts during an acquisition interval could occur when the detector is moving compared to a stationary, single measurement in the middle of the interval. The count-rate of the stationary measurement can be calculated using point-kernel approximation as the total number of counts in the detector, $\dot{N}_{\mathrm{sum}}$, during the same acquisition time. A comparison of simulated measurement time-series obtained while passing a source positioned at 10 m from the trajectory of the detector at a speed of 50 km/h using 1 s acquisition time intervals for the point-kernel approximation and the integrated estimates of the count-rate function are illustrated in Fig. 6.

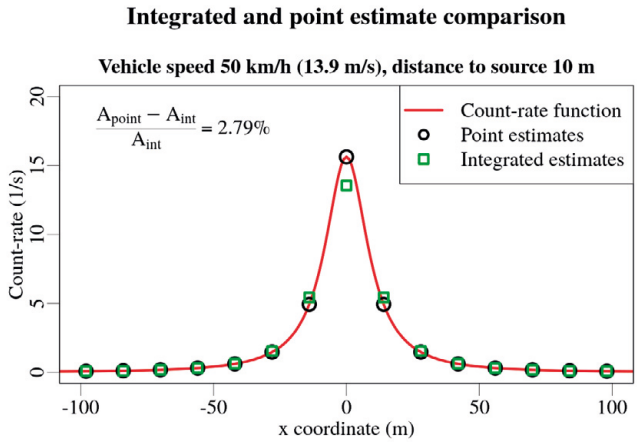

Fig. 6. Comparison of point vs integrated estimates of measurement values of mobile gamma spectrometry data when the source is positioned at 10 m distance from the trajectory of the detector. The red line denotes the count-rate function in the detector; black circles mark the point estimates, and green squares mark integrated estimates. The relative difference of the areas under the point and integrated estimate peaks is 2.79 %. Figure from paper III.

The relative difference of the areas under the point and integrated count-rate estimates, from the example in Fig. 6, yields a value of 2.79 %. Point-by-point differences of the count-rate function estimates can be considerably more significant, reaching 15 %. Examples of point-by-point differences are shown in Fig. 7, for the "best" and "worst" relative alignments of the measurement acquisition intervals and the count-rate function for source distances of 10, 20 and 30 m. As discussed in the section "Peak in the count-rate function", the best alignment occurs when the highest value in the count-rate function coincides with the middle of the measurement time slot, yielding the maximum possible counts in the detector (see Fig. 4). On the other hand, the worst alignment occurs when the highest value of the count-rate function coincides with an edge between two measurement time slots. As can be seen in Fig. 7 this has a significant effect on the point-by-point differences. The greatest deviations being seen for the closest (10 m) sources in the best alignment situation. At 20 m, the maximum absolute point-by-point difference for the best alignment situation has decreased by about three times, from 15 % to less than 5 %, while the reduction for the worst alignment was more minor (from 7 % to 3 %). The discrepancy between the point-by-point differences for varying relative alignments arises from the distance difference between the source and the detector at the start and the end of the acquisition time interval. Because more time during the acquisition time interval in the best alignment situation is spent closer to the source than in the worst alignment situation, a more significant difference in the point-by-point variation occurs.

As the differences are significant only for short distances (smaller than the distance the detector has travelled during the acquisition time interval at a speed of

14 m/s or 50 km/h past the source), point-kernel approximation was used throughout papers I-III for estimating count-rate functions in the detectors. More detailed investigation regarding the effects of approximation on Bayesian estimations is performed in paper III.

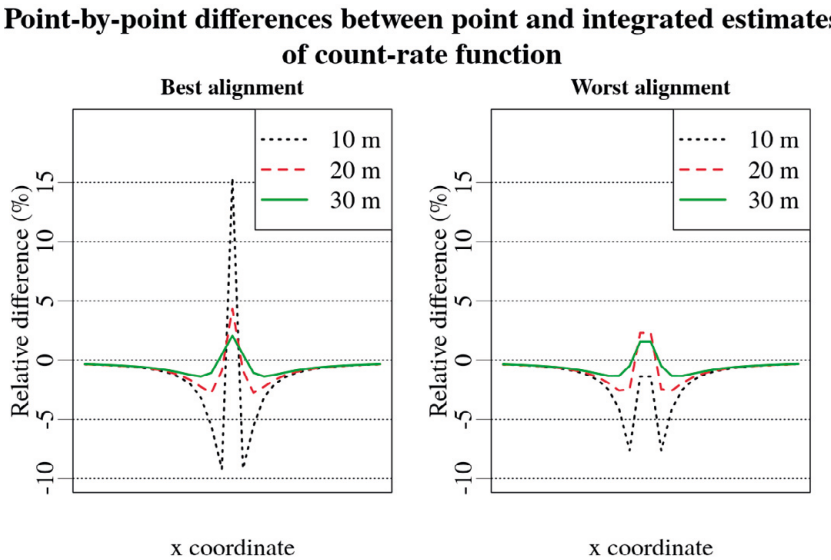

Fig. 7. Comparison of relative point-by-point differences between integrated and point estimates of the count-rate function for best and worst relative alignments. Distance of 10 metres to the source is displayed by black dotted line, 20 metres – red dashed line and 30 metres – green solid line, as indicated in the legends. The speed of the vehicle for this example is 50 km/h. Figure from paper III.

Statistics of radioactive source detection

Usually, to estimate the activity of a radionuclide in mobile gamma spectrometry, registered photons are counted in a full energy peak of the pulse height distribution. A peak in the pulse height distribution is identified, and then the shape of the peak is fitted (usually with a Gaussian distribution) to obtain the net counts in the area of the peak. When searching for lost sources positioned tens of metres away, the number of counts in the full energy peaks is low due to the relatively short amount of time spent in the vicinity of the source. There may be too few counts to enable the gamma spectrometry software to fit the peak with the Gaussian distribution to obtain the peak area. A more straightforward method is often used when the number of counts within a specific photon energy interval (a region of interest, ROI) is small. The total number of counts within the ROI is summed and compared with the background counts in the same ROI. If the number of counts in the ROI is significantly higher than the background counts, c in Eq 16, then a photon source is likely to be in the vicinity of the radiation detection system.

Such a calculation method is fast and reliable and works even if there is no full energy peak in the pulse height distribution [26].

As radioactive decay is a Poisson distributed process, the number of counts detected in a ROI of the pulse height distribution in a specific time interval will follow a Poisson distribution. Thus, the probability for detecting k number of counts when the average number of counts in the detector is denoted by λ can be calculated using the probability mass function of the Poisson distribution:

$$P(X=k)=\frac{\lambda^k e^{-\lambda}}{k!}. \qquad 18$$

The variance, σ^2, of the Poisson distribution is the same as the mean λ, therefore the standard deviation is the square root of variance $\sigma = \lambda^{1/2}$. An illustration of the estimated probabilities of the number of counts in the detector during the selected acquisition time interval for three mean count-rates in the detector (10,20, and 30) is given in Fig. 8.

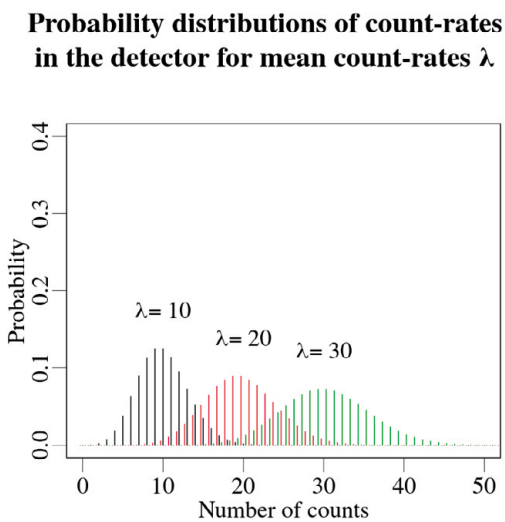

Fig. 8. An illustration visualising the probabilities to register a set number of counts for a given mean number of counts in the detector, denoted by several values of the λ of the Poisson function – 10 (black), 20 (red) and 30 (green).

Because the number of counts in the detector due to the natural background radiation is also Poisson distributed, it is possible to leverage this knowledge and obtain an indication of whether there may be an additional radioactive source nearby. A prevalent method to achieve this is to set a so-called alarm threshold level, visualised in Fig. 9 [20]. This level can be set in many ways, one of which is based on a pre-set number of expected false-positives in a chosen amount of time.

The probability of obtaining not more than k counts in the detector with the mean count-rate denoted by λ can be evaluated using the cumulative distribution function, denoted *CDF*:

$$CDF(k,\lambda)=e^{-\lambda}\sum_{i=0}^{\lfloor k \rfloor}\frac{\lambda^i}{i!}. \qquad 19$$

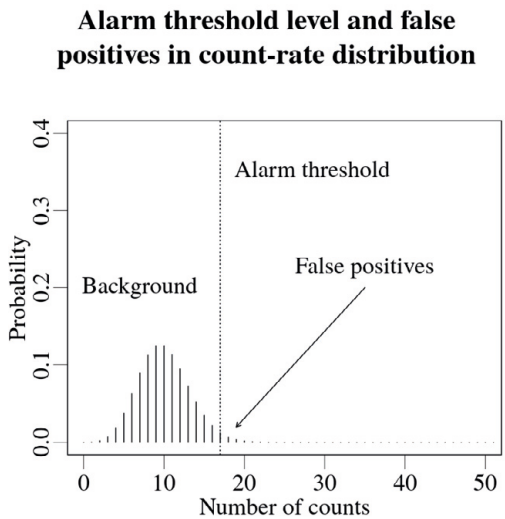

Fig. 9. Illustration of detected false positives due to a mean background count of 10 in the detector and alarm threshold value of 17, displayed by a vertical dotted line. The false positives are to the right of the alarm threshold value.

Thus, the probability of obtaining number of counts greater than k, with λ mean counts in the detector can be written:

$$P_{\text{greater}}(k,\lambda)=1-CDF(k,\lambda). \qquad 20$$

If the alarm level is set low, the probability of detecting a source will increase, but so will also the number of false positives. If, on the other hand, a higher alarm level value is chosen to produce few false positives, the likelihood of detecting a source is reduced. The alarm level setting is thus a compromise between the likelihood of detecting a source and the number of tolerated false positives. For example, by finding such k value that $P_{\text{greater}}=3600^{-1}$, an alarm threshold level for one false alarm per hour is set. Additionally, if there is a varying radiation background, the actual number of false positives within a time interval will change. This might further complicate the choice of a suitable alarm threshold level and affect the results of the orphan source search.

In a scenario, where the source is located close enough to the path of the detector, and the number of photons emitted by the source is adequately elevated above the variation of the background count-rate, c, the count-rate distribution should shift above the alarm threshold level during the passage of the source, indicating a possible presence of a photon source. This is illustrated in Fig. 10.

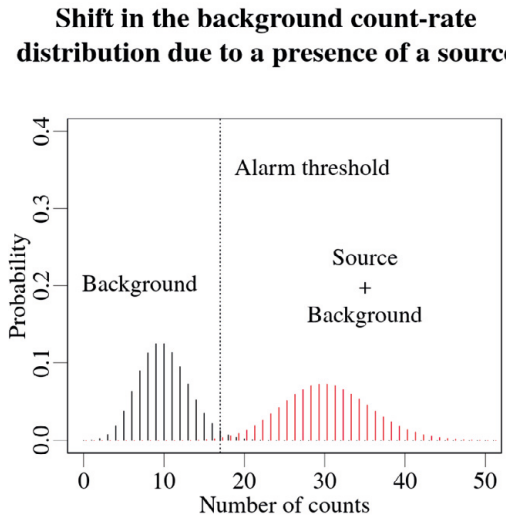

Fig. 10. Illustration of a situation, where the distribution of count-rates shift above the alarm threshold while passing the source.

Bayesian model for estimation of source position and activity

When searching for an orphan source, the parameters of interest are the position, P, and the activity, A, of the source. In this case, the result of the Bayesian inference would be the posterior probability distributions of the position and the activity of the source. Let $\pi(P,A)$ be the prior distribution for those parameters representing the prior knowledge of position and activity in a distributional form. The information to formulate the priors for these parameters (P and A) cannot be obtained from radiation theory, so instead, the information stems from the specific situation. This information could subsequently be the probability of the source being in the area, the number of possible sources, what kind of radiation source it is and where it could be situated. If there is no prior information regarding the position of the radioactive source, an assumption can be made that every position in the two-dimensional area of interest, S, is equally likely. Thus, a uniform distribution over the area of interest S can be chosen, expressing a lack of information regarding the position of the source, P. Similarly, if there is limited information regarding the activity of the source A, a uniform prior for the activity could also be used:

$$A \sim \text{Uniform}\left(A_{\min}, A_{\max}\right). \qquad 21$$

However, such a prior sets bounds on the source activity $A_{\min}$ and $A_{\max}$, which might be undesirable. Additionally, if there is no knowledge about the activity of the source and every value of the activity is possible, uniform distribution is not a good choice because it cannot span through the interval [0,∞) and be integrated to 1, for it to be a proper distribution. Substituting the prior activity of the source to a Gamma distribution, it is possible to overcome the limitations mentioned above. By choosing appropriate values of shape κ and scale θ, a density of Gamma distribution at a point a can be obtained using the expression:

$$\text{Gamma}\left(a, \kappa, \theta\right) = \frac{1}{\Gamma\left(\kappa\right)\theta^{\kappa}} a^{\kappa-1} e^{-\frac{a}{\theta}}, \qquad 22$$

where $\Gamma(\kappa)$ is the value of gamma function for the shape parameter value κ. The domain of the gamma function is $\text{Gamma}\left(a, \kappa, \theta\right) \in \left[0, \infty\right)$. Thus, the prior distribution for activity of the source can be written:

$$A \sim \text{Gamma}\left(\kappa, \theta\right). \qquad 23$$

Because the shape κ and scale θ parameters greatly influence the shape of the distribution, they have to be chosen to have little effect on the posterior distribution – i.e. the posterior is dominated by the likelihood – for the Bayesian model to function correctly. Prior distributions set up in such a way are called "vague priors" and are commonly used in Bayesian statistics when little or no information is known about the parameters of interest [18]. A robustness check must be performed with different sets of parameters to verify that this is the case.

The second component left to complete the Bayesian model is the likelihood, which depicts how well the selected model is supported by the data and the values of parameters of interest in the context of orphan source search. While setting the mathematical model for the likelihood, it is possible to utilise gamma radiation detection knowledge, which is not usually included in the traditional methods of orphan source search. After a detector has passed a radioactive source of activity A, positioned at position P close enough to a number n of measurement coordinates $X = x_1, x_2, ..., x_n$, there will be a visible peak in the measurement time-series of the detector $Z = z_1, z_2, ..., z_n$. If all of the measurement positions X, the source activity A and position P are known, then by utilising Eq. 16 it is possible to estimate the likelihood distribution of the data $\pi\left(Z|X, A, P\right)$, given the selected values of the parameters of interest for the number m of possible detectors:

$$\pi(Z|X,A,P)=\prod_{j=1}^{m}\prod_{i=1}^{n}\mathrm{Pois}\left(z_{i,j}|\lambda=\dot{N}_{\mathrm{sum},i,j}(p,x_{i,j},x_{i-1,j},E_\gamma)\right),$$

$$\dot{N}_{\mathrm{sum},i,j}=\frac{A\,n_\gamma\varepsilon_{\mathrm{ref}}(E_\gamma)\varepsilon_{\mathrm{rel}}(E_\gamma,f_{\mathrm{angle},i,j}(p,x_{i,j},x_{i-1,j}))e^{-\mu_{\mathrm{air}}\|x_{i,j}-p\|}}{4\pi\|x_{i,j}-p\|^2}+c, \qquad 24$$

where m is the number of detectors used and n is the number of measurements.

One can then combine the information of the likelihood (the observations) and the prior (initial knowledge about the parameters) using Bayes formula (Eq. 3):

$$\pi(A,P|Z,X)\propto\pi(Z|X,A,P)\cdot\pi(A,P), \qquad 25$$

The distribution $\pi(A,P|Z,X)$ is known as the posterior distribution. In essence, Bayesian inference utilises the likelihood to produce probability values of the parameters of interest, according to the selected model and input data, and then "filters" the resulting probability distribution using the prior.

Reconstructing the deposited activity on the ground from air-borne gamma spectrometry data

Count-rate in the detector due to fresh fallout

Considering an unshielded gamma-ray point source positioned at some distance r from the detector. The fluence rate at the detector, $\dot{\varphi}$, can be estimated using Eq. 4. Expressing the distance between the source and the detector r in three spatial dimensions, with z denoting the altitude coordinate, yields:

$$r=\sqrt{(x_0-x)^2+(y_0-y)^2+(z_0-z)^2}, \qquad 26$$

where coordinates x, y, and z denote the position of the photon source and x_0, y_0, and z_0 – the position of the detector. It is possible to estimate the fluence at the detector due to fresh fallout by integrating over the coordinates x and y, assuming a contaminated surface with a uniform spatial activity distribution of α [Bq/m^2] spanning along the coordinates x and y. Denoting the number of photon emission from an area $\alpha dxdy$ within the surface, it can be written:

$$\dot{\varphi}(x,y)=\int\int \frac{\alpha\, dx\, dy\, n_\gamma e^{-\mu_{air}\sqrt{(x_0-x)^2+(y_0-y)^2+(z_0-z)^2}}}{4\pi(x_0-x)^2+4\pi(y_0-y)^2+4\pi(z_0-z)^2}. \qquad 27$$

In reality, atmospherically dispersed radioactive material may be more or less uniformly deposited on the ground depending on weather conditions and the type of ground surface [27], [28].

Discrete approximation of the area of interest

Utilising point-kernel integration (PKI) it is possible to approximate an area S, which is a part of the infinite, flat surface area with uniform contamination, with a number n of discrete gamma-ray point sources. Then, the fluence at the detector positioned above the area of interest S can be written:

$$\dot{\varphi}_{\mathrm{PKI}}=\sum_{i=1}^{n} \frac{\alpha_i q\, n_\gamma e^{-\mu_{\mathrm{air}} r_i}}{4\pi r_i^2}, \qquad 28$$

where n is the number of point sources, α_i is the activity per unit area of the i-th point source, q is the area the point source is representing, and r_i – distance to the i-th point source. In PKI approximation using square grid, the area represented by the source q is proportional ($q=l_g^2$) to the distance between the points l_{g}. An illustration of such approximation of a surface area using 100 points with distance l_{g} between the points is displayed in Fig. 11. By setting an arbitrary area spanning $x\in[x_{\min};x_{\max}], y\in[y_{\min};y_{\max}]$, makes it possible to calculate the fluence at the detector positioned within the area at the altitude h, while changing the distance l_g. If the size of the area is significantly larger than the mean free path of the photons in the air, the area can then be approximated as an infinite surface. Then, by calculating the fluence at the detector as a function of distance parameter l_{g}, it is possible to obtain the smallest distance l_{g} for which the fluence from the infinite surface calculated using PKI method will not differ more than minimal from the fluence evaluated using an integration of infinitesimally small volumetric sources.

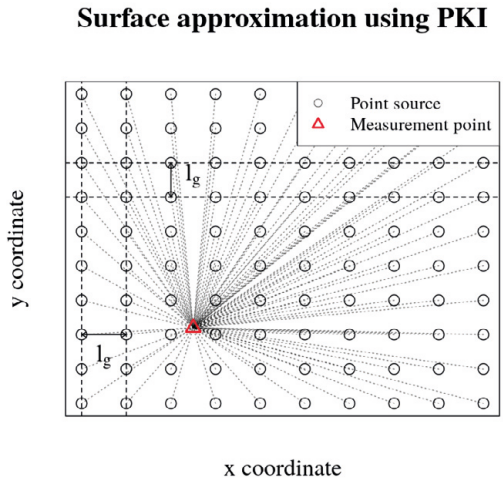

Fig. 11. An illustration of a surface approximated with discrete point sources using PKI method. The discrete sources with distance l_g between them are marked with black circles. The measurement position is marked with a red triangle. Path of primary photons are shown using grey dotted lines to display the effect of all of the sources.

This is visualised in Fig. 12 for altitudes h=1, 5, 10, 15, 30, 50 and 100 m. It can be seen that the PKI approximation is valid even for distances l_g slightly larger than the altitude of the detector h.

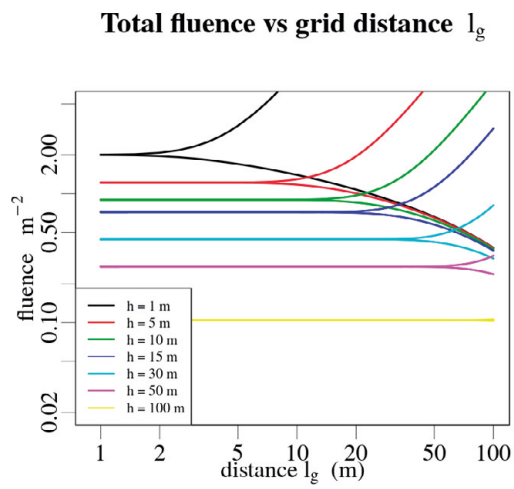

Fig. 12. Fluence variations in a detector above an infinite, plane surface source approximated using PKI for different distances between the grid points l_g and altitudes above the surface h. The diverging lines for a particular height denotes a point at which the calculated fluence will start to vary depending on the relative alignment of the detector and point sources. If a point source happens to be directly below the detector, an increase in the fluence is observed displayed with the upward tending curves. If the detector is above a point between the sources, a decrease in the fluence can be observed. The distance l_g, at which these lines diverge denotes the biggest l_g value which can be used in PKI approximation of a contaminated surface with very little deviations for a given altitude of the detector.

If the survey is being performed with an airborne detector, most probably the lowest practical altitude h of the detector will reach tens of metres to avoid manufactured structures, ground features or foliage. In such circumstances setting the distance l_g to a much shorter length than the minimum altitude of the detector during the survey will not increase the accuracy or the spatial resolution of the measurements.

Detector response function when reconstructing the deposited surface activity

Let us now consider an infinite surface with uneven distribution of a radionuclide on the surface. We are interested in the activity deposited per unit area in a selected area of interest S. Using the PKI it is possible to approximate the area of interest S using a number n of equally distributed point sources of activity per unit area $\alpha_i = \alpha_1, \alpha_2, \ldots, \alpha_n$, being a discrete representation of a continuous distribution of the deposition density, α_{dep} (Bq/m2). In such a situation, the fluence at the detector at some position above the surface S with distance r_i to the i-th source point can be obtained using Eq. 28. The fluence can then be expanded for a number m of measurement points, which for the j-th measurement can be written:

$$\dot{\varphi}_j = \sum_{i=1}^{n} \frac{\alpha_i n_\gamma q e^{-\mu_{air} r_{i,j}}}{4\pi r_{i,j}^2}. \qquad 29$$

When performing measurements using an unmanned aerial vehicle (UAV) or any other airborne gamma spectrometry (AGS) vehicle, successive measurements are made while the spectrometry system is moving around the survey area, usually in a predetermined path reminiscent of a grid [29]–[32]. The outer bounds of the grid usually coincide with the edges of the area of interest, and often the measured count-rate values are interpolated to obtain a "radiation map" of the area of interest, depicting count-rate at the altitude of the detector [28], [33], [34]. Thus, it can be assumed that the extent of the area of interest is known when the measurement itinerary throughout the area is planned, with the outer edges of the measurement grid delineating the area of interest. An example of such trajectory is shown in Fig. 13. Then, by populating the area of interest with point sources arranged so that the distance between the point sources is not greater than the altitude of the detector, it is possible to obtain the positions of the point sources in relation to the measurement points. The distances $r_{i,j}$ between each point source i and each measurement point j can be calculated. Then, for the point sources inside the area of interest a detector response function R_{inside} for a given photon energy E_γ can be quantified, using the counting efficiency of the detector; that will express the influence of each point source on the detector count-rate:

$$R_{\text{inside}}(E_\gamma) = \frac{n_\gamma q\, \varepsilon(E_\gamma) e^{-\mu_{\text{air}}(E_\gamma) r_{i,j}}}{4\pi r_{i,j}^2}, \qquad 30$$

which is a dimensionless function. The response function can also be expressed in a matrix form for number n of point sources and number m of measurements:

$$R_{\text{inside}} = \begin{bmatrix} R_{1,1} & R_{1,2} & \dots & R_{1,n} \\ R_{2,1} & R_{2,2} & \dots & R_{2,n} \\ \dots & \dots & \ddots & \dots \\ R_{m,1} & R_{m,2} & \dots & R_{m,n} \end{bmatrix}, \qquad 31$$

where each element of the matrix represents the count-rate in j-th measurement point due to the i-th point source per decay.

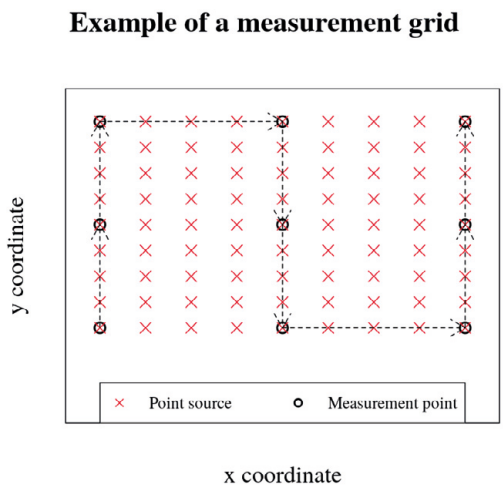

Fig. 13. Illustration of a square measurement grid, with arrows displaying the path through the area. Point sources are marked by red × symbols, and the measurement points are denoted by black circles.

Then, by linearly multiplying the inside response matrix by an activity vector α, denoting the activity per unit area of each point source, the count-rate in the detector at each position j can be evaluated:

$$\begin{pmatrix} \dot{N}_1 \\ \dot{N}_2 \\ \vdots \\ \dot{N}_m \end{pmatrix} = \begin{bmatrix} R_{1,1} & R_{1,2} & \cdots & R_{1,n} \\ R_{2,1} & R_{2,2} & \cdots & R_{2,n} \\ \cdots & \cdots & \ddots & \cdots \\ R_{m,1} & R_{m,2} & \cdots & R_{m,n} \end{bmatrix} \begin{pmatrix} \alpha_1 \\ \alpha_2 \\ \vdots \\ \alpha_n \end{pmatrix}. \quad 32$$

Or more simply:

$$\dot{N}_{\text{inside}} = R_{\text{inside}}\, \alpha. \quad 33$$

Having the detector response function available makes it very easy to evaluate the count-rate in the detector at the measurement points. Although this is trivial for the geometry considered in this section, in practice it may be difficult to evaluate the response function for an area due to e.g. uneven terrain, shrubs, trees or man-made structures. It might be that it is sufficient to use geographical coordinates obtained from the GNSS receiver to obtain a rough approximation of the response function for cases where great accuracy of the predicted deposition density is not needed. In situations where spatial accuracy and resolution is required, especially for non-horizontal surfaces, additional methods to obtain information about the environment is needed, such as light detection and ranging (LIDAR) [35], [36]. After evaluation of the response function, plotting the individual count-rate values $\dot{N}_j$ in a "heat-map" results in a fallout map for the area. Further in this thesis, the detector response function discussed previously will be denoted "inside detector response function".

It has to be noted, that the detector response function in Eq. 30 describes a situation when the surface contamination is only inside the area of interest. If the area of interest is a small part of a greater area, which subsequently has surface contamination throughout this greater area, the detector response function represents the situation incorrectly. It is visualised in Fig. 14 – when calculating the count-rates due to a uniform surface contamination a drop in the count-rate when approaching the edges, or even more so – in the corners, can be observed.

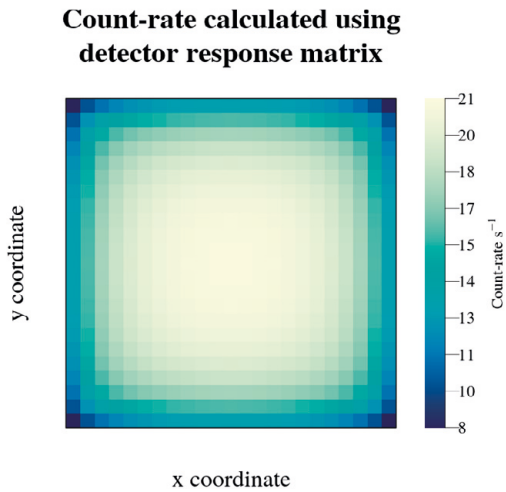

Fig. 14. An example of count-rate values calculated for a square area of interest using only detector response function. The count-rate scale is displayed on the right

This happens because per unit angle of photon incidence, the count-rate from the surfaces right below the detector makes up only a small part of the total count-rate [37]. This is visualised in Fig. 15, where fluence (proportional to count-rate) is displayed per vertical angle (angle of 0 degrees points directly downwards), for altitudes of the detector h=1, 10, 30, 100 and 200 m [37]. To obtain count-rate values representing a situation, where the area of interest is only a small part of a larger area that is contaminated by surface deposition, an additional detector response matrix for point sources outside the area of interest has to be estimated.

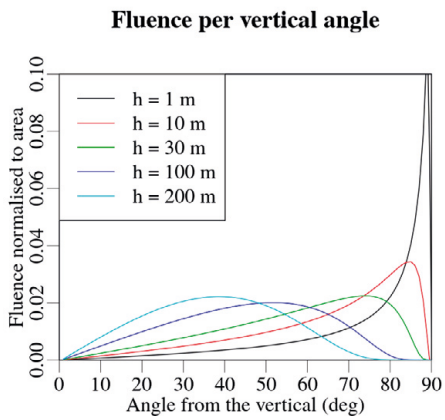

Fig. 15. Fluence per vertical angle for different altitudes of the detector [37]. Angle of 0 degrees points directly downwards, angle of 90 degrees – to the horizon, parallel to the surface.

Detector response for point sources outside the area of interest

To be able to correctly estimate the count-rate due to a surface source inside an area of interest, which is a part of a larger area with surface contamination, detector response function for point sources outside of the area of interest must be evaluated. To evaluate this "outside detector response function", the source approximation grid is expanded by several hundred metres, away from the edges of the area of interest *S*, as displayed in an example in Fig. 17. Then, the outside detector response function can be evaluated using similar methodology as discussed in the previous section "Detector response function when reconstructing the deposited surface activity". If there is a number *u* of such outside point sources, then applying Eq. 30 for the outside point sources it is possible to obtain the outside detector response function:

$$R_{\text{outside}} = \begin{bmatrix} R_{1,1} & R_{1,2} & \cdots & R_{1,u} \\ R_{2,1} & R_{2,2} & \cdots & R_{2,u} \\ \cdots & \cdots & \ddots & \cdots \\ R_{m,1} & R_{m,2} & \cdots & R_{m,u} \end{bmatrix}, \qquad 34$$

The matrix elements of the R_{outside} describe the count-rate in all of the measurement points due to all of the point sources outside of the area of interest per decay.

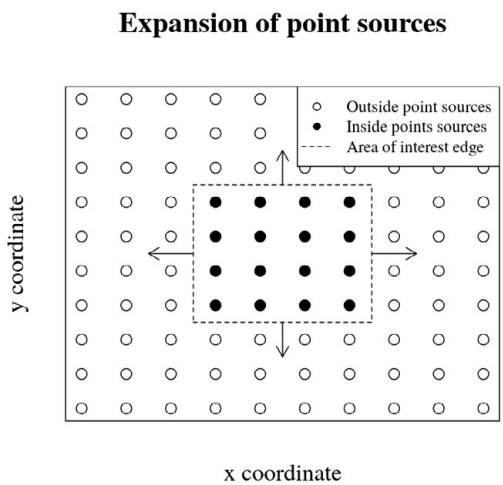

Fig. 16. Expansion of the point sources towards the outside of the area of interest.

Then, assuming that the surface deposition outside of the surface area is uniform, the total count-rate in the detector due to a fresh surface fallout can be

approximated by summing the count-rate due to the sources inside the area of interest S and the count-rate due to the sources outside the area. Assuming that an average activity per unit area value $\bar{\alpha}$ throughout the area of interest represents the activity per unit area of the outside area, it can then be written:

$$\dot{N}_{\text{total}} = R_{\text{inside}}\,\alpha + \bar{\alpha}\,R_{\text{outside}}\,. \qquad 35$$

Adjustment in the model due to the radionuclide deposition depth

When contaminated areas are surveyed sometime after the initial fallout, a gradual depth migration of the fallout may have occurred [38]. If the time since the deposition and the type of material onto which the radionuclides were deposited can be estimated, then the deposition depth can also be roughly evaluated [37]. To estimate the fluence at the detector in such circumstances correctly, the path that the photon has travelled in the material onto which radionuclides had been deposited has to be evaluated. A simple depth profile model was chosen, consisting of a radioactive plane covered with an inactive slab of material of thickness d_{dep} (Fig. 17).

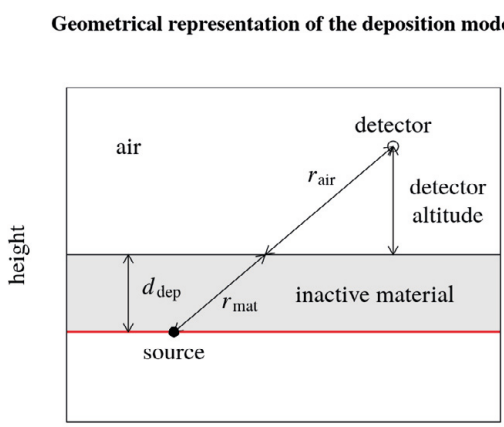

Fig. 17. A graphical representation of the deposition model used.

Then, considering a uniform planar surface deposition on the ground covered with an inactive layer of thickness d_{dep} having a mass attenuation coefficient for photons μ_{mat} and density ρ_{mat}, the fluence at the detector can be estimated using:

$$\dot{\varphi}_j = \sum_{i=1}^{n} \frac{\alpha_i n_\gamma q^2 e^{-\mu_{\text{air}} r_{\text{air}\,i,j}} e^{-\mu_{\text{mat}} \cdot \rho_{\text{mat}} \cdot r_{\text{mat}\,i,j}}}{4\pi \left(r_{\text{air}\,i,j} + r_{\text{mat}\,i,j} \right)^2}, \qquad 36$$

where $r_{\text{air}\,i,j}$ is the distance in air and $r_{\text{mat}\,i,j}$ is the distance in the material the emitted photon has travelled from the i-th "surface deposition point" to the j-th measurement point due to the deposition depth d_{dep}. By substituting this fluence formulation while estimating R_{inside} and R_{outside} of the UAV borne detector, possible penetration depths of the deposition of the radionuclides in to the soil or other surfaces can be taken in to account.

Bayesian model for estimating the surface radionuclide distribution

Suppose we want to obtain the spatial radionuclide distribution on the ground per unit area α. In that case, the posterior distribution $\pi(\alpha|Z)$ is then composed of probability distributions of activity per unit area of each of the surface deposition elements in the area of interest S, given the measurements Z:

$$\pi(\alpha|Z) \propto \pi(Z|\alpha)\,\pi(\alpha). \qquad 37$$

The prior $\pi(\alpha)$ describes the information that is available before performing the measurements in a distributional form. In a radiological emergency, it could be set according to the expected levels of contamination in that particular emergency situation. Stemming from the Eq. 35, the likelihood is set as:

$$p(Z|\alpha) = \prod_{i=1}^{n} \text{Pois}\left(z_i | \lambda = R_{\text{inside}}\,\alpha_i + \bar{\alpha} R_{\text{outside}} \right). \qquad 38$$

Then, the prior and the likelihood are combined using Eq. 37.

A brief introduction to Markov chain Monte-Carlo

Trying to evaluate a posterior distribution either for an orphan source situation described in section "Bayesian model for estimation of source position and activity" or for estimation of radionuclide distribution within an area of interest described in "Bayesian model for estimating the surface radionuclide distribution" is not straightforward. In both situations the posterior distribution is a complex and explicit, thus it is not possible to make any direct inferences from it. To obtain samples representing the posterior target distribution an indirect sampling using Markov chain Monte-Carlo (MCMC) was used [39]. The MCMC algorithm was written in a language and environment for statistical computing **R** [40].

MCMC is a method generating theoretically independent samples from the target distribution. Throughout the thesis, a particular variant of the MCMC methods is utilised, referred to as the Metropolis-Hastings (MH) algorithm [18]. This MH method can be applied to a broad spectrum of problems [41]–[48]. Due to the universality of the Metropolis-Hastings algorithm, it is relatively slow compared to other, more specialised variations of the MCMC methods like Hamiltonian Monte-Carlo [49]. In the basic form, the MH algorithm is as follows:

1. Let $f(x)$ be a function that is proportional to the desired probability distribution $P(x)$.
2. Choose an arbitrary point x_0 to be the first sample and choose an arbitrary probability density $g(x|y)$ that serves as a proposal distribution, suggesting a candidate for the next sample value x, given the previous sample value y.

For each iteration t:

3. Generate a candidate x' for the next sample by picking from the distribution $g(x'|x_t)$.
4. If g is symmetric: i.e $g(y|x) = g(x|y)$, then calculate the acceptance ratio $\alpha = f(x')/f(x_t)$. Otherwise, $\alpha = f(x')\, g(x_t|x')/f(x_t)\, g(x'|x_t)$.
5. Generate a uniform random number $u \sim \text{Uniform}[0;1]$
6. If $u \leq \alpha$, then accept the proposal by setting $x_{t+1} = x'$
7. If $u > \alpha$, then reject the proposed value and set $x_{t+1} = x_t$

This algorithm provides a framework to more efficiently sample multivariate posterior distributions for multiple parameters of interest. Each additional parameter of interest adds another dimension in the posterior distribution, from which then samples have to be correctly drawn.

For each parameter of interest, the sequence of MCMC samples throughout the selected number of iterations t_{max} is called an MCMC "chain". Each individual chain has to be started with an initial parameter. Then, starting from this initial parameter the chain will start to move towards an area in the posterior distribution which has a higher probability, further converging to the point of the highest local probability. An illustration of an MCMC chain is displayed in Fig. 18.

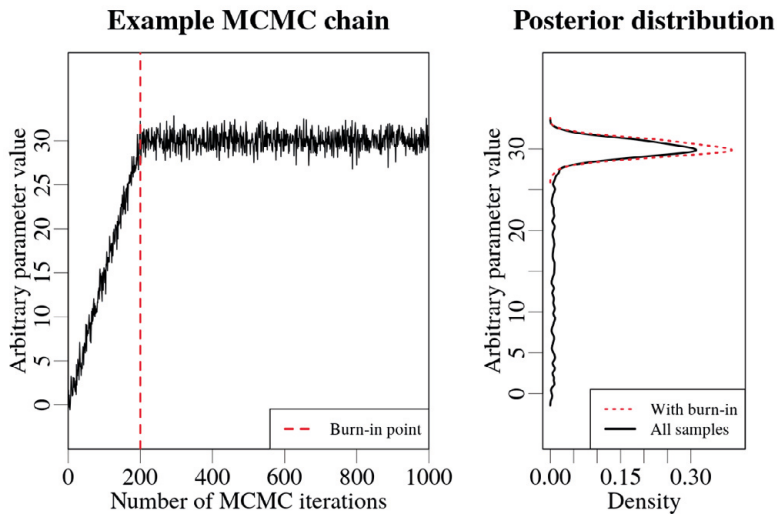

Fig. 18. An example of a trace plot of an MCMC chain (left) with the resulting posterior distribution (right). A hypothetical burn-in point denoting when the MCMC chain has arrived at the maximum probability point is marked by a vertical dashed red line. The posterior distribution made up of all the samples in the posterior is marked by a black curve. The posterior distribution with the burn-in (discarding the first samples not representative of the distribution) is marked by a red dotted curve.

The number of iterations required for the chain to converge depends on the variance of the proposal distribution. The smaller the variance, the more iterations are needed. Increasing the variance of the proposal distribution increases the convergence speed. If the variance of the proposal distribution is increased too much, the proposed values might jump over the highest probability point in the posterior distribution and thus subsequently get rejected. Thus, over-increasing the variance of the proposal distribution will drastically increase the number of iterations needed for the chain to converge. This is reflected in acceptance rate AR, denoting the ratio of the number of accepted proposals N_{acc} to the number of MCMC iterations N_{sim}:

$$AR = \frac{N_{\text{acc}}}{N_{\text{sim}}}. \qquad 39$$

Too low or too high an acceptance rate will lead to an inefficient sampling of the posterior distribution. For problems with a high number of dimensions (>5), an acceptance rate of 0.24 is considered the most efficient [39], [50]. Regardless of the acceptance rate, it will still take a finite number of iterations for the chain to reach the maximum probability point as illustrated in Fig. 18. Because of this, the first samples in the posterior are not representative of the posterior distribution and are

usually discarded. The number of discarded samples is denoted by *burn-in* [18]. Usually, it is the first few thousands of the samples.

After a sufficient number of iterations, the obtained samples should represent the target distribution sufficiently well. The number of iterations required depends on the variance of the proposal distribution, as that will dictate how fast the chain arrives at the point of highest probability and how efficient will the sampling of the posterior be. Generally, if the chain becomes stationary as in Fig. 18, it can be said that the chain has converged. The more samples the chain will obtain after convergence, the more accurate the representation of the target distribution will be.

Usually, efficient MCMC algorithms are tailored to a specific problem. This might potentially lead to a poor performance of the MCMC algorithm if the input data has changed considerably. It is possible to change the dynamics of the MCMC chain by altering the size of the proposal distribution while the MCMC is running. Such self-regulating algorithms are called adaptive MCMC algorithms, utilised to speed up the convergence of the MCMC chains [51], [52].

Material and methods

Mobile gamma spectrometry vehicle – Papers I-IV

A gamma spectrometry system was set up in a service bed compartment of a customised Chevrolet Silverado pickup truck, illustrated in Fig. 19. The system consisted of three ionising radiation detectors: one HPGe-detector with a relative efficiency of 123%[1] mounted in a special holder in the centre of the back portion of the service bed at the height of 1.5 m above the ground, and two 4-l NaI(Tl) detectors mounted to a suspended rail system attached to the roof of the service bed compartment on the right side of the truck. The NaI(Tl) detectors were mounted one in front of the other, and will subsequently be referred to as the front NaI(Tl) detector (NaI F) and the rear detector (NaI R). The HPGe-detector was connected to a DigiDART multichannel analyser (MCA), which was set up with 2048 channels. The NaI(Tl) detectors had DigiBASE MCAs mounted directly to the photomultiplier tubes inside the detector casing, using 1024 channels. All of the MCAs and a G-STAR IV GNSS receiver (BU-353S4) were connected to a computer using the Nugget software [53].

Fig. 19. An image of the open service bed portion of the mobile gamma spectrometry vehicle used throughout the thesis. The 123% HPGe detector with a cryostat can be seen in the back of the service bed, with the sensitive medium of the detector pointing to the back of the vehicle. The two blue boxes in the top of the right side of the service bed are the 4l NaI(Tl) detectors. The GNSS receiver is mounted on the roof of the cabin of the car. Figure from paper II.

[1] Counting efficiency relative to a 76×76mm NaI(Tl) crystal at 1.332 MeV

Measurement data from gamma spectrometers in this vehicle is used in manuscripts I, III and IV. The theoretical model describing the angular variations of counting efficiency of the detectors present in the vehicle alongside their offsets relative to the GNSS receiver is documented in manuscript II and also described below.

Measurement of angular variations of detector efficiency

The angular efficiency response of the mobile gamma spectrometry system was measured on a patch of pavement near the village Löddeköpinge in Sweden. A rectangular coordinate system (18 m × 11 m) was defined (Fig 20). Along the edges of the defined rectangular coordinate system, 40 points for placing sources were chosen, with distances between the points of 1.5 m, except for the distance between the last step along the shorter axis that was 0.5 m. The measurement set-up resulted in an angular resolution of roughly 10 degrees.

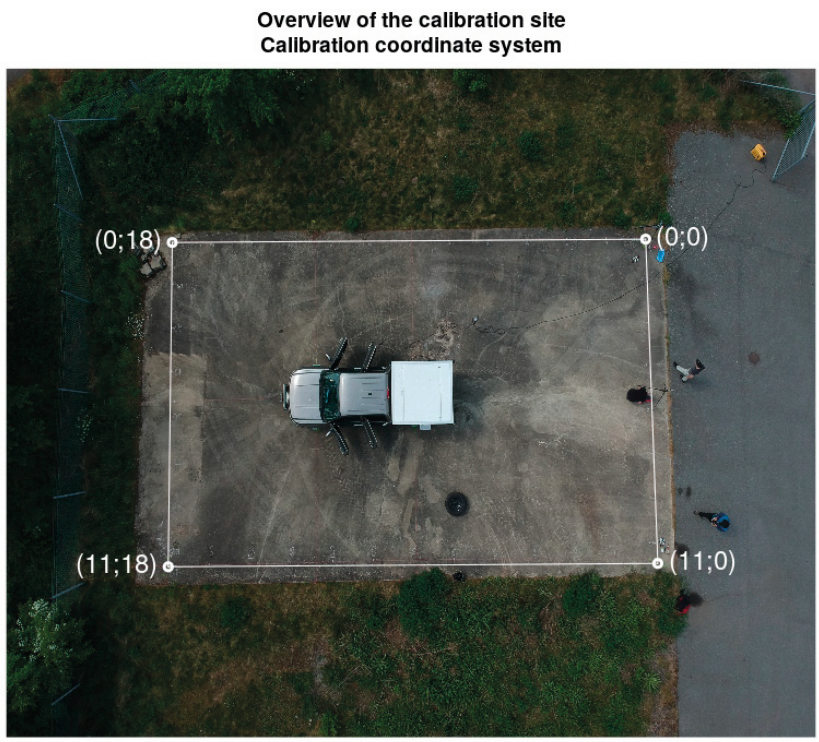

Fig. 20. An overview of the positioning of the vehicle inside the defined coordinate system. Figure from paper II.

The vehicle was positioned in the centre of the patch so that the detectors inside the service bed of the vehicle were reasonably close to the centre of the coordinate system. During the measurements, the vehicle was fully operational, with lid and cabin doors closed and operators present in the cabin. The calibration was performed for two radionuclides separately – ^{60}Co and ^{137}Cs, using calibration sources of activity 34.1 ± 1.2 and 66.5 ± 2.1 MBq respectively. One at a time, the calibration sources were situated in each measurement position for 2-3 minutes. Pulse height distributions in the three individual detectors (123% HPGe, 2x4l NaI(Tl)) were then collected simultaneously. Full energy peak areas in the pulse height distribution obtained from each detector were evaluated manually. Then, using the areas of the full energy peaks N_{FEP} in the pulse height distributions, the counting efficiency for every measurement position and radionuclide was calculated using the equation:

$$\varepsilon = \frac{N_{FEP}\, 4\pi r^2}{A\, n_\gamma e^{-\mu_{air} r} t} \qquad 40$$

where r is the distance between the detector and the source and t is the measurement time. Individual positions of the sensitive medium of the detectors in the coordinate system were used when calculating the actual distance between the source and the detector. The resulting angular variations of counting efficiency for the [0;360) degree interval were then interpolated for every 10 degrees.

Because both NaI(Tl) detectors had no structural components hindering their performance at 90 degrees relative to the driving direction of the vehicle, the relative angular efficiencies were normalised to their 90-degree values. As structural pillars at the back of the service bed were obstructing the HPGe detector in the regions of 90 and 270 degrees (Fig. 19), it was chosen to normalise the relative efficiency of the HPGe-detector to the 80-degree value. The resulting normalised relative angular variations of counting efficiencies are displayed in Fig 21 for ^{60}Co and ^{137}Cs. Reference efficiency values measured at 90 degrees from the detectors are given in Table 1.

Table. 1. Selected ROIs in the gamma spectra and their respective reference efficiencies for the ^{137}Cs and ^{60}Co radionuclides for different detectors used in the mobile gamma spectrometry vehicle. Adapted from paper II.

Detector	^{137}Cs		^{60}Co	
	ROI (keV)	Ref. Eff. (m^2)	ROI (keV)	Ref. Eff. (m^2)
123 % HPGe	658-665	0.0021	1327-1337	0.0015
Front NaI(Tl)	600-750	0.254	1247-1470	0.0166
Rear NaI(Tl)	600-750	0.0261	1247-1470	0.0172

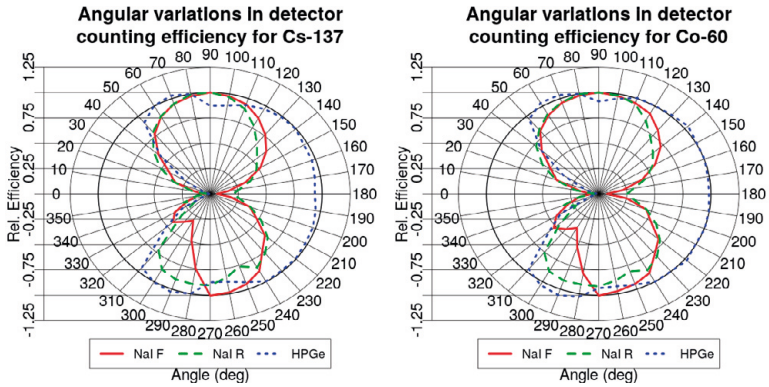

Fig. 21. Angular variations in counting efficiency of the HPGe (blue dotted curve), front NaI(Tl) (red solid curve) and rear NaI(Tl) detectors (green dashed curve) for ^{137}Cs (left) and ^{60}Co (right). The angle of 0 degrees is the driving direction of the vehicle. A slight dip in the counting efficiency of the HPGe detector at 90 and 270 degrees can be seen due to the structural pillars of the service bed. Figure from paper II.

Nugget software

The data in the experiment was recorded using Nugget software, created by Swedish Radiation Safety Authority [53]. The program was designed to aid in mobile gamma spectrometry tasks – recording the measurement data to the computer, analysing the data with possibilities of using various background stripping, alarm threshold values, visualising of the data using waterfall plots, pulse height distributions, measurement time-series in a set ROI or plotting a set parameter on a map. An illustration of the main window of the software is displayed in Fig. 22 below. Because Nugget was written in Visual Basic, there are some limitations regarding the real-time functionality of the software, which will be briefly mentioned here.

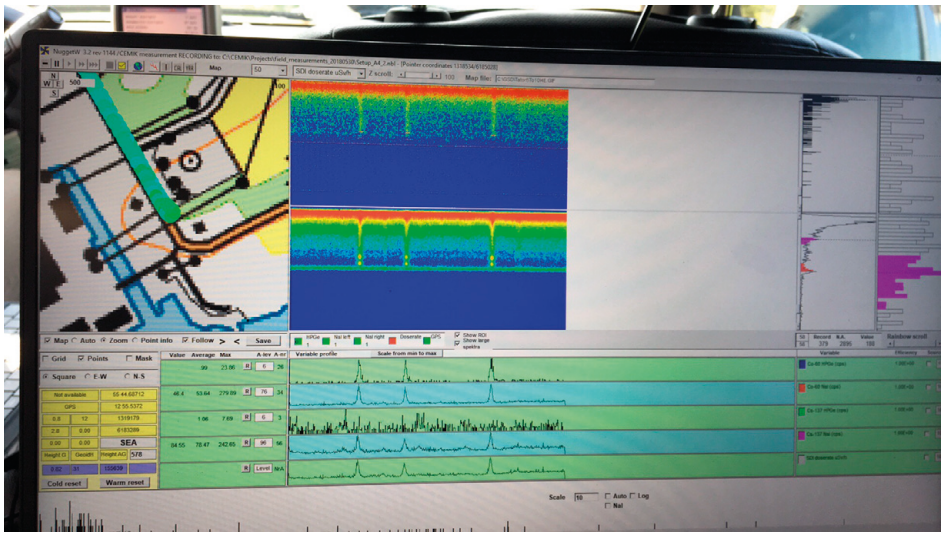

Fig. 22. The main window of Nugget software. The geographical overview of the situation with previous measurement coordinates is displayed in the top-left. The waterfall plots for HPGe (top) and combined NaI(Tl) (bottom) detectors are displayed in the middle, with their corresponding most recent spectra on the right. The measurement time-series for the count-rate values in the selected ROI's is displayed below the waterfall plot.

The main program sequence when Nugget works in acquisition mode is made up of a repeated action set which initiates i) a new measurement acquisition interval in each detector, ii) a reading of the geographical coordinate from a GNSS receiver, after the chosen acquisition time has passed, iii) an ending of the measurement acquisition interval in each detector and iv) a reading of the data from the detectors, v) saving the measurement data to the computer storage, vi) analysing the data based on the settings of the program and vii) visualising the data on the screen. Each of these actions, except waiting for the selected acquisition time to pass, takes a finite, but comparatively small amount of time. A software clock regulates when these actions are performed. If the clock is working as expected the program flow and its subsequent result will be as intended. However, in a case where this clock is not functioning correctly, the relative timing of the events of the program can be altered and thus lead to discrepancies between the actual measurement coordinate and the recorded GNSS coordinate.

If a GNSS receiver is updating the geographical coordinate at a stable time interval and Nugget then is reading this coordinate at varying intervals which might be slightly longer or shorter, the GNSS receiver might not have updated or alternatively – has already updated the coordinate. In such situation it might happen that some measurement coordinates are reported twice and some are jumped over, as displayed in Fig. 23. The authors of the software had been informed about the behaviour and there is now an algorithm in the software slightly compensating for this behaviour, but a solution that completely eliminates the

problem has not been found yet. The potential effect of this mismatch will be discussed more in Paper III.

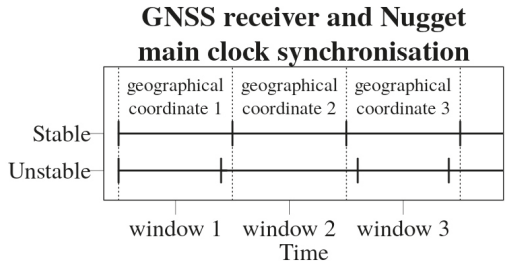

Fig. 23. Relative alignment of the GNSS update interval, displayed by vertical dashed lines, and the Nugget geographical coordinate readout during the acquisition mode, displayed by a short vertical bar on the line. At the top of the graph, a stable situation is displayed, when the Nugget read-out happens regularly and each measurement corresponds to a new geographical coordinate – reported coordinates are 1,2,3,4 and so on. In the bottom of the graph, an unstable situation is displayed, leading to reporting coordinates 1,1,3,3, etc.

Position and activity estimates from a posterior distribution

After the MCMC algorithm has ran for enough iterations, the obtained samples should represent the target probability distribution for the parameter of interest. When utilising Bayesian methods throughout the rest of this thesis and in the papers, the following method was used to define the "estimated" or "predicted" value: a maximum a posteriori (MAP) point within the obtained probability distribution (posterior) is chosen, such that the point has the largest probability within the probability distribution. This is visualised in Fig. 24 below.

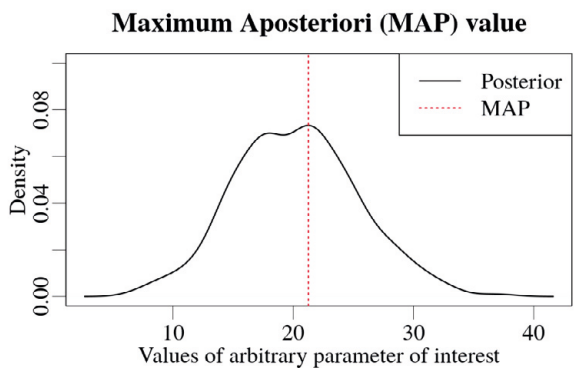

Fig. 24. An example of a posterior distribution (black) and a maximum aposteriori (MAP) value of the posterior distribution (red dotted line).

Paper I

In this paper, a feasibility test for using Bayesian inference on the mobile gamma spectrometry data was performed. An experiment was conducted on a 10.4 km closed road loop near the shut-down Barsebäck nuclear power plant, about 20 km north of Malmö city in southern Sweden. Gamma-ray point sources were set up at different places and distances from the side of the road. The sources were ^{133}Ba, ^{137}Cs and ^{131}I with corresponding activities 183±48, 468±57 and 298±63 MBq, respectively. The distances from the sources to the roadside were 32±1, 32±1 and 62±1 m, respectively.

The mobile gamma spectrometry vehicle was then driven along the road loop past the sources five times at 50 km/h. The pulse acquisition time was set to 1 s, so that each second, a pulse height distribution and a geographical coordinate of the vehicle position was collected. Counts in the ROIs for ^{137}Cs (661.6 keV), ^{131}I (364.5 keV) and ^{133}Ba (356.0 keV) were obtained. The background level, c, was estimated as a mean of selected count-rates obtained in a particular run during the experiment, to imitate online usage of the method. In the first paper no correction was done for the varying angular efficiency of the detectors $\varepsilon(E_\gamma)$ (Eq. 10). Only measurements made at distances greater than 200 m from the positions of other sources were considered to minimise the influence of other sources on the estimations. The likelihood equation used in the Bayesian model for paper I is:

$$\pi(Z|X,P,A)=\prod_{i=1}^{n}\mathrm{Pois}\left(z_i|\lambda=\frac{A n_\gamma \varepsilon e^{-\mu_{\mathrm{air}}\|p-x_i\|}}{4\pi\|p-x_i\|^2}+c\right). \qquad 41$$

where z_i is the i-th measurement of counts in the selected ROI, p and x_i are two-dimensional predicted source and i-th measurement coordinates respectively.

The Bayesian algorithm was run for 30 000 iterations with a burn-in of 10 000 iterations. After a successful run, the algorithm outputs posterior distributions for source position and activity. The predicted distance, D, to the source was defined as the distance between the position with the largest probability and the measurement position of the maximum number of counts in the measurement time-series. Predicted activity values were obtained by calculating the maximum a posteriori (MAP) values of the posterior distributions for source activity. The predicted distance and activity values were compared to the actual values.

AUTOMORC experiment set-up – Papers II-IV

An experiment studying the detection limits of various detection systems was performed by positioning ^{60}Co (emitting two gamma photons of energy 1.1732 and

1.3325 MeV per decay) and ^{137}Cs (emitting one gamma photon of 0.6617 MeV per decay) sources at two positions along the road in a designated experiment area. At each position, the sources were placed at various distances from the road. The experiment was carried out on a relatively straight stretch of one-lane road (approximately 1.7 km long), at the same site as in the experimental study for Paper I. It involved 20 different experimental set-ups, at which point sources of ^{137}Cs and ^{60}Co with five different activities for each radionuclide were used. The experimental set-ups were divided into groups of four. In each group, the sources had the same activity but were gradually moved further away from the road side. The vehicle was then driven along the road past the two source positions.

The exact distances from the roadside and the activities of the sources in all the experimental set-ups are shown in Fig. 25. Actual distances from the sources to the detectors when the vehicle was closest to the detectors was about two metres longer due to the additional distance from the road side to the centre of the lane of the road the vehicle was driving in.

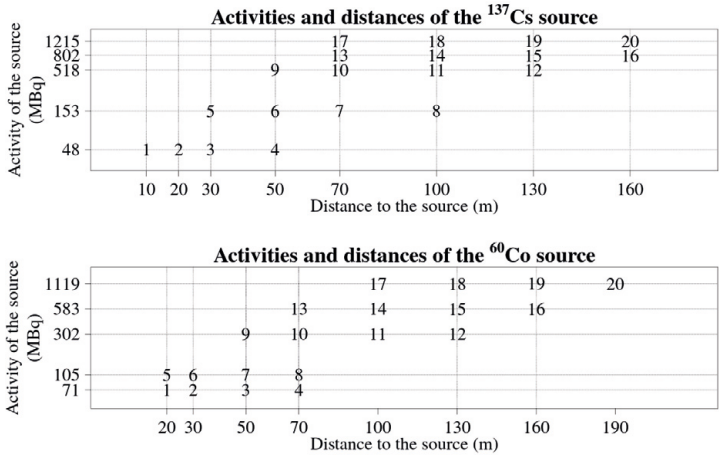

Fig. 25. Distances from the roadside to the ^{137}Cs and ^{60}Co sources and activities of the sources used in the experiment for each set-up. The numbers in the graphs represent the experimental set-up number. The actual distance from the sources to the detectors was about two metres longer. Figure taken from paper III.

The sources were placed in the defined positions for about 10 minutes for each experimental set-up. During this time, the gamma spectrometry vehicle was driven back and forth along the road, passing the gamma-ray sources several times.

Evaluation of accuracy and precision of the Bayesian estimations in papers II and III

In the following papers II and III, posterior distributions of position and activity of the source were obtained after 30 000 MCMC iterations with a burn-in of 10 000 iterations. Then, the estimated positions and activities were analysed in groups according to the radionuclide, detector combination and experimental set-up. Estimated values were extracted from the posterior distributions as described in section "Position and activity estimates from a posterior distribution". Relative deviations *RD* of the estimated positions and activities of the sources were calculated for each pass of the source individually. The relative deviations, *RD*, were calculated as below, where *EST* is the estimated value, and the *REF* – selected reference value:

$$RD = \frac{(EST - REF)}{REF} \qquad 42$$

In the Eq. 42 above, the *REF* values for position and activity were the actual position and activity values. This is common for both Papers II and III, although in paper II, the relative deviations were denoted differently: Activity relative deviation (ARD), position relative deviation (PRD), etc., despite the underlying formula being the same. In paper III the notation was simplified, where the relative deviation of source position was also divided in to lateral (perpendicular to the road) and longitudinal (along the road) deviations, in order to get more detailed information about the estimated positions of the sources. The notation across papers II and III is clarified in Table 2.

Table. 2. Clarification of the notation across papers II and III.

Notation in Paper II	Notation in Paper III	Meaning
ARD	Relative deviation of source activity	Relative deviation of median value of estimated source activity values for a given experimental set-up.
PRD	Relative deviation of source position	Relative deviation of median value of estimated source position values for a given experimental set-up.
ARDD	–	Distribution of ARD values throughout the experimental set-ups
PRDD	–	Distribution of PRD values throughout the experimental set-ups
–	Relative deviation of longitudinal source position	Relative deviation of median value of estimated source position values along the road throughout a given experimental set-up.
–	Relative deviation of lateral source position	Relative deviation of median value of estimated source position values across the road throughout a given experimental set-up.

These values were then used in the analysis of the performance of the algorithm by plotting the relative deviations as a function of SNR of the data.

Paper II

The second paper aimed to theoretically test the Bayesian algorithm's capabilities, using synthetic data free from the possible experimental uncertainties affecting experimental data. Angular variations of efficiency and the possibility to utilise data from multiple detectors were introduced into the Bayesian model according to Eq. 24. To obtain a measure of the variation in the performance of the algorithm, it was chosen to perform estimations of activity and position of the sources using six different variations of the algorithm and then comparing the estimated values to the actual ones. The six variations of the algorithm tested in paper II are as follows:

1. using simulated data (z_i Eq. 24) only from the HPGe detector with a fixed counting efficiency (ε_{rel} in Eq. 24 is set to a fixed value);
2. using data only from the HPGe detector using angular variations in counting efficiency (ε_{rel} in Eq. 24 represents the relative angular efficiency of the detector);
3. using data only from the front 4l NaI(Tl) detector with a fixed counting efficiency;
4. using data only from the front 4l NaI(Tl) detector using angular variations in counting efficiency;
5. using data from all of the detectors present in the vehicle (123% HPGe, 2x4l NaI(Tl)) with a fixed counting efficiency for all individual detectors;
6. using data from all of the detectors present in the vehicle using individual angular variations in counting efficiency for all of the detectors

Synthetic data

The synthetic data was simulated by taking a random sample from a Poisson distribution, with λ_i of the Poisson distribution representing the mean number of counts (Eq. 18) in a detector at a measurement point i per unit of time t. Geographical coordinates obtained using a GNSS system of one complete pass from the AUTOMORC experiment were chosen as the central coordinates in the successive simulated time-slots of the pulse acquisition. The background count-rate c for each ROI of the selected radionuclides and individual detector was evaluated as a mean value of counts in these selected ROI obtained from the pulse height distribution recorded in the AUTOMORC experiment while driving along the

predetermined path in the absence of any radioactive sources. The mean number of counts at every measurement position i were calculated by applying the activity and position of the source corresponding to a selected experimental set-up (Fig. 25) and average background level c using the equation Eq 16. Angular variations in the counting efficiencies of primary gamma photons for all three detectors were included in the calculation of the synthetic data alongside the individual offset of each detector from the position of the GNSS receiver antenna on the vehicle.

A total number of 10 Poisson distributed synthetic N_{sum} time-series in the detectors for each type of source in source set-ups were calculated to evaluate the algorithm's average performance. The modelled data series were then used as an input into the Bayesian algorithm. To compare the discrepancies in the results more accessibly, signal-to-noise ratios (SNR) were calculated for all individual set-up and source combinations. SNRs were calculated as a ratio between the maximum amplitude of $\dot{N}_{\text{source}}$ and the standard deviation of the background count per second, c. Henceforth, the following formula was used in the calculations:

$$\text{SNR} = \frac{\max\left(\dot{N}_{\text{source}}\right)}{\sqrt{c}}, \qquad 43$$

Bayesian algorithm

The Bayesian algorithm described in paper I was further developed in four aspects:

- Angular variations in counting efficiency were added;
- Individual positional shift depending on how the specific detector was mounted in car relative to the position of the GNSS receiver was implemented;
- Ability to utilise data from multiple detectors at the same time introduced;
- Improved proposal generation mechanism, to more accurately sample the bimodal posterior probability distribution of the position of the source, covered in section "Improvement of bimodal distribution sampling".

Each of these aspects improved the Bayesian estimations by altering the Bayesian model to reflect the actual situation more closely or improving the MCMC algorithm to obtain a correct posterior distribution.

The first three points were achieved by modifying the likelihood equation for the Bayesian model. The resulting likelihood was:

$$\pi(Z|X,A,P)=\prod_{j=1}^{m}\prod_{i=1}^{n}\mathrm{Pois}\left(z_{i,j}|\lambda=\dot{N}_{\mathrm{sum},i,j}\left(p,x_{i,j}x_{i-1,j},E_{\gamma}\right)\right),$$
$$\dot{N}_{\mathrm{sum},i,j}=\frac{An_{\gamma}\varepsilon_{\mathrm{ref}}\left(E_{\gamma}\right)\varepsilon_{\mathrm{rel}}\left(E_{\gamma},f_{\mathrm{angle},i,j}\left(p,x_{i,j},x_{i-1,j}\right)\right)e^{-\mu_{\mathrm{air}}\|x_{i,j}-p\|}}{4\pi\|x_{i.j}-p\|^{2}}+c \qquad 44$$

where i is the measurement number and j is the detector number (number m of detectors and n of measurements). Setting the likelihood as in Eq. 44 allows to have as many detectors as needed and takes in to account individual angular variations of counting efficiency and individual offset for each detector j.

Improvement of bimodal distribution sampling

Because detectors used in the vehicle do not register the angle of incidence of the incident photon, the correct general solution to the source localization problem given measurements obtained while travelling past a source is therefore *a bimodal distribution*, with possible position on either side of the road/vehicle direction. The fact that the starting coordinate for the MCMC chain is in the middle of the two local maxima of the posterior distribution for the source position, there is a tendency of the MCMC algorithm to stay within the side of the road towards which the first jump was made. Irrespective of whether there is additional information (arising due to angular variations of the counting efficiency, detector position offsets, etc.) or not, the algorithm will most probably stay on the side of the road/vehicle direction chosen with the first step if the proposal distribution is only generating proposals on one side of the road. This limits the ability of the algorithm to sample the full bimodal distribution correctly. Thus, the position of the proposal coordinate is mirrored to the opposite side of the road each 1 000 MCMC iterations as a possible solution.

Paper III

Continuing with the studies of the limits of the Bayesian algorithm for orphan source search, in the following article it was logical to test the modified algorithm on experimental data. The data used were obtained in the experiment AUTOMORC, which is described in section “AUTOMORC experiment set-up – Papers II-IV” above.

Because it was found that incorporation of the angular variations in the counting efficiency of the detectors did improve the estimates, however slightly, it was

decided to test only three variations of the algorithm, all including the angular variations of counting efficiency:

- using data (z_i in Eq. 24) only from the HPGe detector using angular variations in counting efficiency (ε_{rel} in Eq. 24);
- using data only from the front 4l NaI(Tl) detector using angular variations in counting efficiency;
- using data from all of the detectors present in the vehicle using individual angular variations in counting efficiency for all of the detectors.

Uncertainty in the measurement coordinates

As mentioned previously the Nugget software has consistently been used in the studies of this thesis for reading the data from the GNSS receiver and the detectors, and then analysing and visualising the results for each new measurement. Due to peculiarities mentioned earlier in how Nugget is programmed in the section "Nugget software", the timing of the read-out of the coordinates from the navigation system is affected, manifesting as discrepancies between the recorded and the actual coordinates of the measurement. Intercoordinate distance analysis (distance between adjacent measurements) for experimental set-up 5 in Fig. 26 visualises these discrepancies. During the experiment, the vehicle was driven back and forth along the road past the sources at a constant speed of about 50 km/h (13.9 m/s) using automatic speed control system in the vehicle. At the end of a complete pass, the vehicle was then turned around, and another pass of the sources was made. As can be seen in Fig. 26, the fluctuations in the intercoordinate distances are implying that the speed of the vehicle was sometimes erratically increasing or decreasing, despite the fact that the speed of the vehicle was constant. All of this translates to longitudinal (along the path of the vehicle) shifts of the measured coordinate, as seen in Fig. 26. If such discrepancies in longitudinal position were to occur in a vicinity of a radioactive source, recorded values of the count-rate would be assigned incorrect coordinates, distorting the shape of the peak in the measurement time-series exemplified in Figs. 5-6.

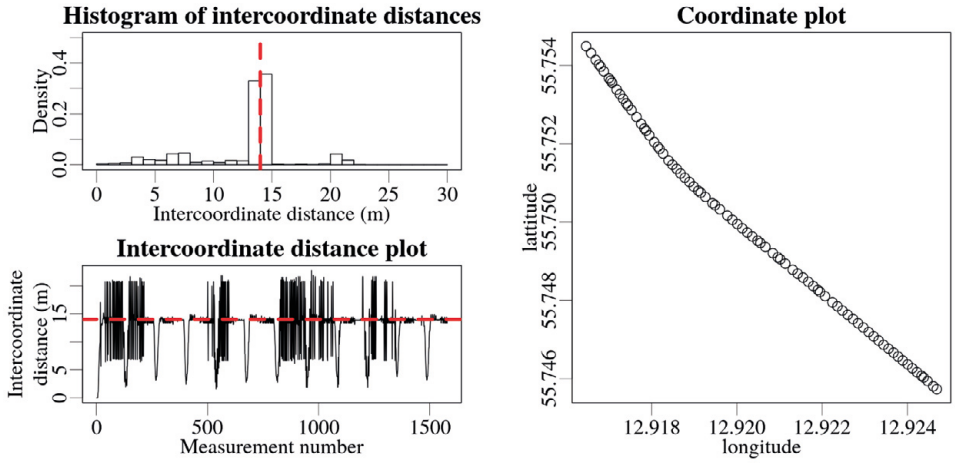

Fig. 26. Intercoordinate distance analysis of the geographical coordinates recorded and processed by the Nugget software for experimental set-up 5 of AUTOMORC experiment. The graph in the upper-left shows a histogram of the length of intercoordinate distances. The lower-left graph shows the intercoordinate distance values for each measurement. The average speed of the vehicle during the experiment was 50 km/h (13.9 m/s), indicated by the red dashed lines. The longitude-latitude graph on the right illustrates a small portion of one of the many passes of the sources recorded in the data displayed on the left, where fluctuations in the recorded coordinate position along the path of the vehicle are clearly visible. Figure from paper III.

It was decided to roughly estimate how much such discrepancies would affect the Bayesian estimates. A method for approximately simulating the discrepancies was reverse-engineered using the experimental data. A function modifying coordinates based on the observed coordinate discrepancy patterns in experimental data was developed, which is explained in more detail in paper III. Coordinates along a 2 km line with 13.9 m/s distance between the coordinates, corresponding to 1 s pulse acquisition time, were calculated. For every coordinate a synthetic count-rate value due to a source positioned at d=30 m away from the nearest point of the trajectory of the detector was calculated. Then, the coordinates, for which the count-rates were calculated, were altered using the reverse-engineered method. Bayesian estimates were then evaluated for the synthetic data with unaltered, correct coordinates and with the altered coordinates with injected discrepancies.

Paper IV

A widely adopted methodology for orphan source detection using mobile measuring equipment and alarm threshold values is based on previously described detection statistics in section “Statistics of radioactive source detection”. Combinations of particular detectors, vehicle speed and detection statistics yield a maximal distance at which an unshielded photon point source can be detected at a certain probability. The fourth paper describes a computational model (the MDD

algorithm) for calculating these maximum detection distances and the knowledge stemming from the model. The model can estimate the maximum detection distance for a single stationary measurement and a mobile pass of a source in a straight trajectory. Calculated results were validated using the experiments described in the section "AUTOMORC experiment set-up – Papers II-IV".

The MDD algorithm was programmed in Fortran 90. The calculation routine is described in paper IV. To check the correctness of the code, two programmers independently wrote the core functions of the algorithm in R-script. Calculated results from the three versions showed agreements within about one percent. The deviations can be attributed to differences in the numerical precision, such as calculation step lengths and the number of iterations.

Paper V

Moving from the orphan source detection problem to that of two-dimensional mapping of radioactive deposition over surfaces, the aim of the fifth paper was to explore the applicability of Bayesian methods for reconstruction of spatial distribution of radionuclides within an area using gamma spectrometry measurements made with an UAV-borne spectrometry system. A contaminated area representing a typical Swedish neighbourhood was modelled using a Monte-Carlo particle transport simulation code SERPENT 2 [54], [55].

SERPENT model of a typical Swedish neighbourhood

The model consisted of 15 houses and a street, spanning 140 × 140 m, as visualised in Fig. 27, left. The houses were single-floor buildings 10 × 15 m in size. The wall heights were 2.95 m high, with the apex of gable roofs reaching 4.95 m height (Fig. 27, right). The rest of the model area was soil.

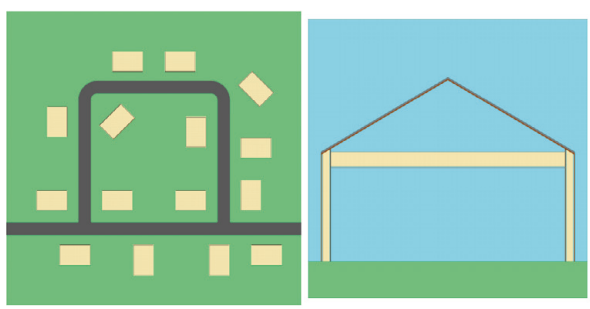

Fig. 27. A top-down schematic view of the model of the neighbourhood based on work by Hinrichsen et al. [56]. The houses are displayed in light-yellow colour, the street – dark grey and the soil – light-green (left). A cross section of a house with the gable roof visible (right). Images adapted from [55].

A ground deposition of 100 kBq/m^2 of ^{137}Cs in the soil was modelled in the neighbourhood, with the ground contamination being distributed uniformly over a 5 cm soil depth. The contamination level for the streets was set lower – 50 kBq/m^2 with a deposition depth of 0.5 cm. The roofs of the houses had the lowest contamination level of 40 kBq/m^2 with 0.1 cm deposition depth. For all of the materials (soil, streets and roofs) the depth distribution of radionuclides was uniform within the deposition depth. This set-up corresponds to the reference deposition scenario, referred to as the clean-up scenario 0 in the Table 3. Three other clean-up scenarios were defined, depicting different extents of decontamination for different surfaces of soil, street and roofs of the buildings (Table 3). Then, primary photon fluence rate in 30 × 30 × 30 cm voxels spanning the whole 140 × 140 m area was calculated for altitudes of h = 6, 10 and 15 m using 10^9 simulated particles in Serpent.

Photons that managed to reach the spatial limits of the 140 × 140 m area were transported to the opposite side of model. The direction and the energy of such photons was not altered, only the position. This corresponds a situation where the neighbourhood is surrounded by exact copies in all directions.

The calculations resulted in fluence matrices of 460 × 460 elements for each altitude of the voxels h. Due to computational limitations, the resolution of these fluence matrices was reduced to 10 × 10 elements yielding 100 surface deposition points, which is enough for a proof-of-concept study. An example of a full resolution 460 × 460 "heat-map" of fluence matrix obtained in the voxels at 6 m altitude of the detector for cleanup scenario 0 is displayed in Fig. 28. The reduced fluence matrix was then regarded as the measurement values obtained using a fictive sensor, that has a proportional response to the fluence of 662 keV photons in the voxels.

Then, the activity per unit area of these surface deposition points were estimated with the Bayesian algorithm using the reduced fluence matrix as the input data.

Table. 3. Descriptions of different clean-up (or decontamination) scenarios with amount of relative reduced surface deposition of ^{137}Cs for particular surfaces.

Cleanup scenario	Ground	Street	Roof
0	0 %	0 %	0 %
1	0 %	0 %	100 %
2	0 %	100 %	0 %
3	50 %	100 %	100 %

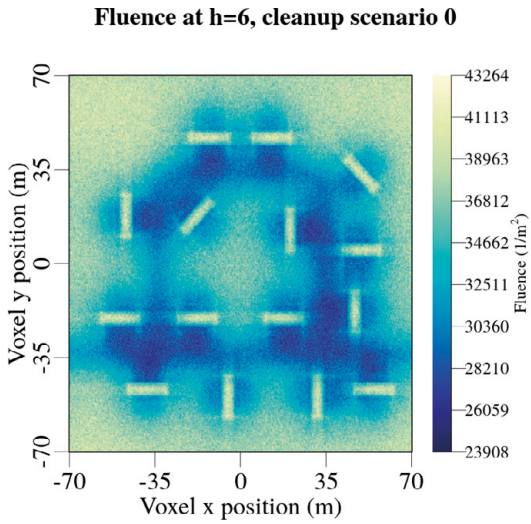

Fig. 28. Fluence of ^{137}Cs primary photons in 30 x 30 x 30 cm voxels at 6 m altitude obtained in the SERPENT 2 model.

Results

Paper I. A Bayesian method to localize lost gamma sources

Paper I was essentially a feasibility test, verifying whether it is possible to obtain information regarding the position and activity of the source from experimental data using Bayesian statistics. The experimental data used in the paper covers only three radionuclides; ^{133}Ba, ^{131}I and ^{137}Cs positioned at 30 to 60 m away from the roadside and having activities of 183±48, 468±57 and 298±63 MBq respectively. Only measurement data from a mobile HPGe detector was used as input to the Bayesian algorithm. The vehicle passed the sources five times. The posterior distributions of source activity and position were evaluated for each source. An example of posterior distributions for source position and activity is displayed in Fig. 29.

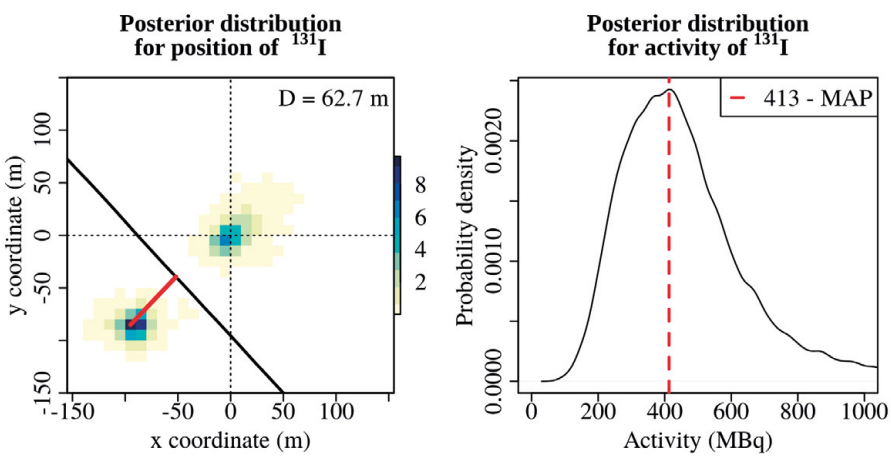

Fig. 29. Example posterior distributions of source position (left) and activity (right). The darker the shade of the colour in the posterior for source position, the higher the probability for source being there. Red line marks the distance from the point in the posterior distribution with the highest probability to the position where maximum number of counts during the passage of the source was detected. The estimated value of activity of the source is marked by a dashed red line. Figure from paper I.

Estimated activity and source distance values were compared to the actual values. It was found that, on average, the algorithm was underestimating the activities of ^{137}Cs, ^{133}Ba and ^{131}I sources by 51%, 15% and 8% respectively. The mean values of predicted source distances were 23, 30 and 63 metres, compared to the actual distances of 32±1, 32±1 and 62±1 metres respectively. It was noticed, that the algorithm was especially sensitive to the shape of the peak in measurement time-series. When performing multiple passes of the source, the recorded number of counts might differ due to statistics, leading to different shapes in measurement time-series (an example is displayed in Fig. 30.)

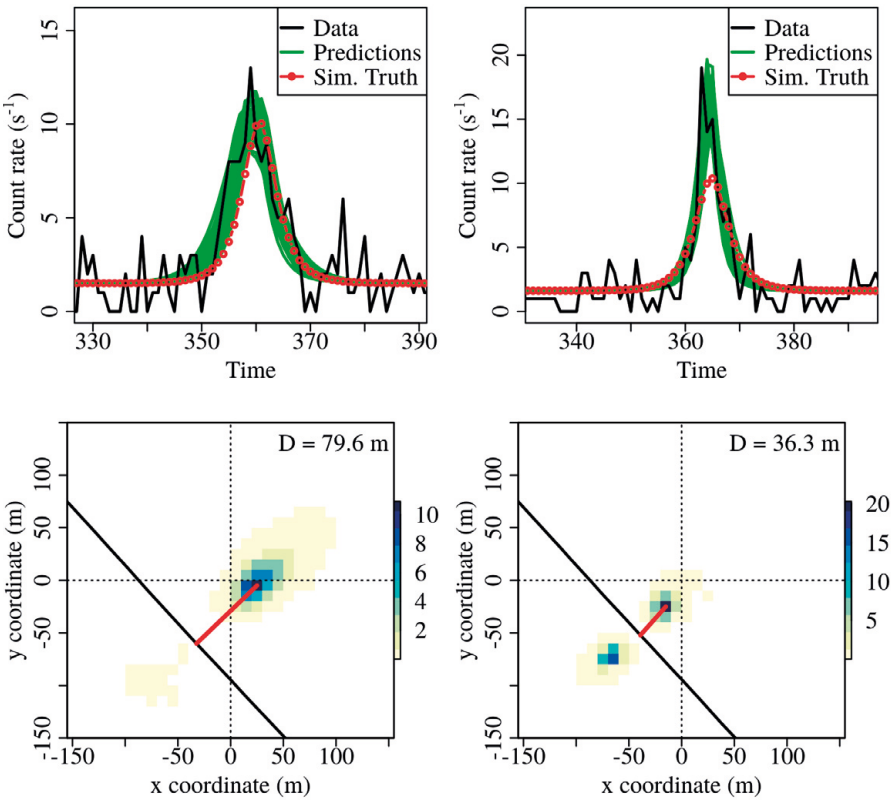

Fig. 30. An example of the influence of counting statistics on the results of the Bayesian method. Measurement time-series of the data recorded by 123% HPGe detector used in the study from two passes (left, right) of the ^{131}I source is displayed with a black line (top). Differences between the measured data is purely statistical. Calculated count-rate function for the measurement positions given the actual source position and activity is displayed with a red dotted line, denoted “Sim. Truth” in the legend, which is the same for both figures – left and right. Green lines represents different predictions of the Bayesian algorithm at different MCMC iterations. Posterior distributions for source position are displayed in bottom left and right from the same runs accordingly. It is obvious, that inferring the position of the source from the wider peak in the measurement time-series results in estimations further away from the road. Figure from paper I.

The main limitations of the Bayesian model used in the first paper were that it was based on three assumptions: there is only one gamma-ray point source of a given radionuclide, the background radiation is constant in the survey area, and that there are no angular variations of the counting efficiency of the detector. Regardless of the limitations, the presented Bayesian method could be utilised for orphan source search as-is, providing predictions of activity and position of the probable source. As the method only requires post-processing of the data, it could potentially be used for analysis of data obtained with other mobile gamma spectrometry systems.

Further work on the influence of angular variations in the counting efficiency of the vehicle detector system, the actual uncertainties resulting from the GNSS unit, and the performance of the algorithm in situations involving more sources at different distances in higher and variable levels of background was considered.

Paper II. Bayesian algorithm to estimate position and activity of an orphan gamma source utilizing multiple detectors in a mobile gamma spectrometry system

The aim of paper II was to theoretically investigate the improvements in the Bayesian estimations of the position and activity of a gamma-ray point source due to the introduction of data from multiple detectors with angular counting efficiency variations.

Based on the simulated data, it appears that the performance of all six individual variants of the algorithm (described in the section "Paper II") in terms of estimating the activity and position of the source, is acceptable for use for one-pass orphan source search situations. It was found that the variant of the algorithm where data from all three detectors were used, and where the angular variations in the counting efficiency of individual detectors was accounted for, could, on average, predict the position and activity of the sources with less than 20 % and 10 % deviations respectively. It became evident that the precision and reliability of the Bayesian estimations depend mainly on the SNR of the data, as illustrated in Fig. 31 below.

Unsurprisingly, the larger the combined efficiency of the detectors present in the mobile gamma spectrometry system, the lower the SNR threshold of the system below which the estimations start to deviate strongly. Threshold SNR levels, at below which significant deviations start to occur were 8, 5 and 3 for variations of the algorithm using data from only HPGE, only NaI(Tl) and all of the detectors correspondingly. Thus, to obtain more reliable and precise position and activity estimations in cases where the activity of the source is near the detection limit, a detector system with better efficiency is required. Alternatively, if there is no time

constraint on the survey but the counting efficiency of the equipment (or sensitivity of the detection systems) is severely limited, additional passes could be performed to increase the amount of information collected for the same SNR level of the data and using the same equipment.

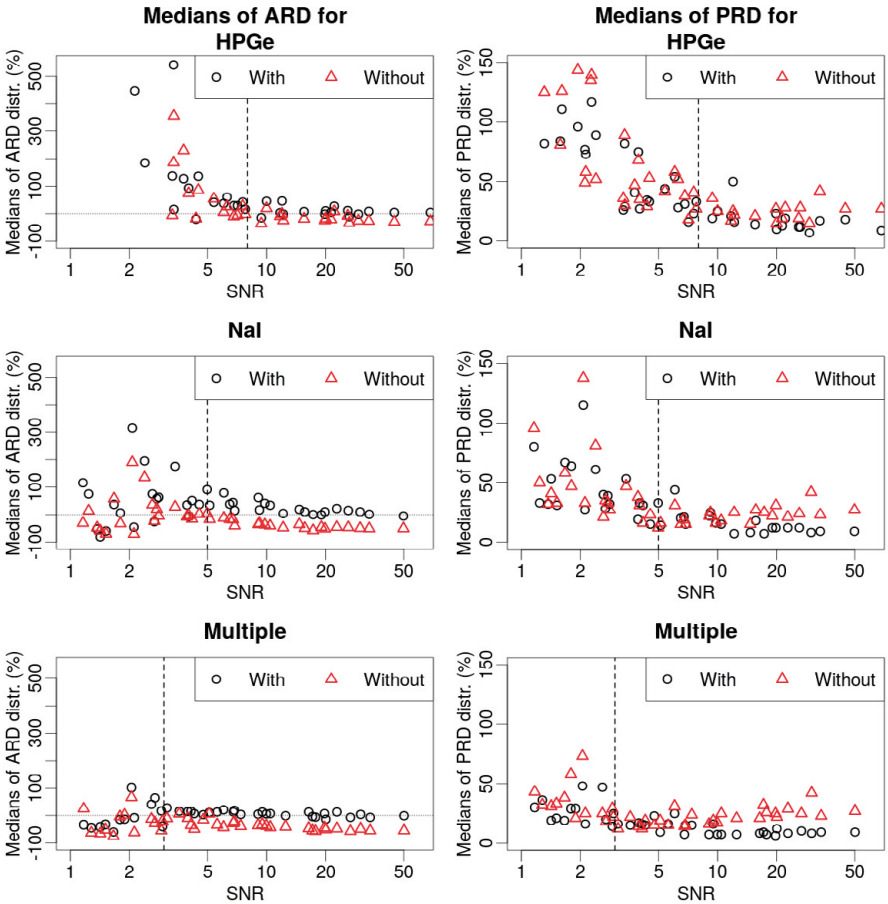

Fig. 31. Medians of activity (ARD, left) and position (PRD, right) relative deviation distributions plotted against SNR values for respective experimental set-ups and radionuclides. Variations of the algorithm using different data were separated into different graphs (HPGe, NaI, Multiple), with and without the use of angular variations of counting efficiency. Horizontal line in ARD graphs marks the 0% relative deviation—actual source activity. Vertical line in all of the graphs marks the approximate individual threshold level for the variations of the algorithm using specific type of the data. Figure taken from paper II. For definitions of ADR and PDR refer to Paper II and Table 2.

From the figure above (Fig. 31), it is evident that inclusion of the angular variations in the counting efficiency of the detectors in the Bayesian model partially corrects the underestimation of the activities as visible in Fig. 21. For example, for the variant of the algorithm utilizing data from all of the detectors, the

50 % underestimation of activity values activity in SNR region 5-50 is corrected (bottom left, Fig. 21).

In emergency situations where such extensive calibration of detector efficiency is not feasible, single values for counting efficiency of the detectors can yield similar results if calibrated properly. Exclusion of the angular variations of counting efficiency from the Bayesian inference would lead to faster performance due to less code in the MCMC part of the algorithm.

Paper III. Accuracy of a Bayesian technique to estimate position and activity of orphan gamma-ray sources by mobile gamma spectrometry: Influence of imprecisions in positioning systems and computational approximations

After the theoretical study in paper II, one of immediate follow-up questions regarding the performance of the Bayesian algorithm is how sensitive the algorithm is to the uncertainties arising in the experimental data. The aim was thus to evaluate the effects of uncertainties present in the experimental data on the accuracy and precision of the estimates obtained using the Bayesian algorithm developed in papers I and II.

If the summed counting efficiency of the detector combination (123 % HPGe, 2x4l NaI(Tl)) is taken into account by linearly combining the SNR values of the data for the 3 detector variant of the algorithm, there is very little difference between the performance of the three algorithms in terms of the dependence of size of the deviations as a function of SNR of the data. This suggests that the performance of the algorithm per efficiency of the detector is very similar.

It is evident, that decreasing SNR of the data (particularly around SNR 3-5) yields in an increase of deviations to 50 – 100 % or more, similar to the Fig. 31 from paper II, where synthetic data was used. For well-detected sources with signal-to-noise ratios (SNR) exceeding 20, activity (Fig. 32) and position (Fig. 33) deviations from actual values were around 30 %. A higher SNR of the data did not significantly improve precision or accuracy of the estimations.

Roughly half of the uncertainty in the position estimation is expected to be due to to the uncertainty in the longitudinal coordinate (distance along the road) and the other half due to the deviations in the lateral coordinate (distance perpendicular to the road).

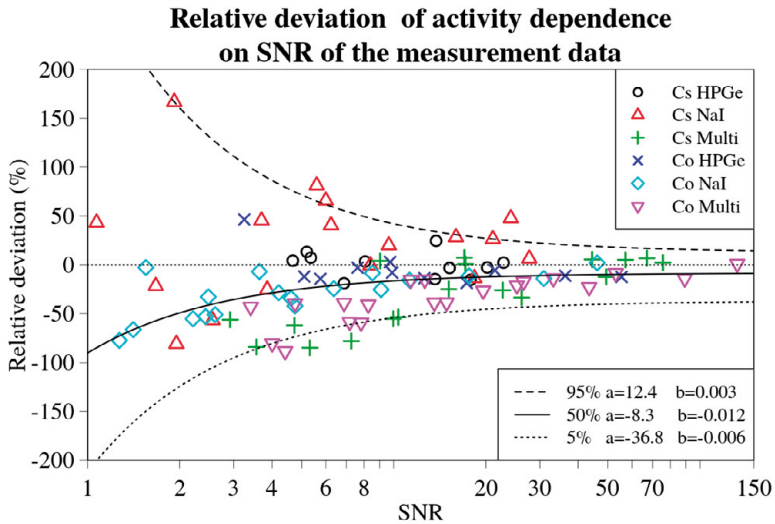

Fig. 32. Relative deviation of source activity for every experimental set-up, detector and source combination plotted against the respective SNR values. Black dashed curve denotes the 5%, solid curve – 50% and dotted curve – 95% (from top to bottom) curves denoting corresponding quantile dependencies on SNR of the data, obtained using non-curvear quantile regression. Fitted parameters *a* and *b* of the curves are displayed in a legend on the right. Figure from paper III.

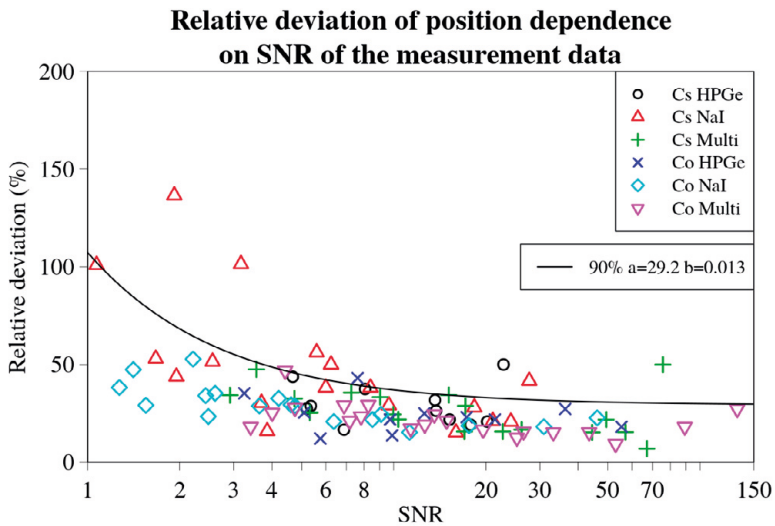

Fig. 33. Relative deviation in source position for every experimental set-up, detector and source combination plotted against the respective SNR values. Black curve denotes a curve representing the 90 % quantile dependency on the SNR of the data obtained using non-curvear quantile regression. Fitted parameters *a* and *b* of the curve are displayed in a legend on the right. Figure from paper III.

If the GNSS receiver cannot provide geographical coordinates at a better resolution than the distance the vehicle has travelled during the acquisition time (14 m here), the uncertainty in the Bayesian predictions will increase. Also, as predicted theoretically in section "Point-kernel approximation of mobile measurements" (Fig. 6), the effects of using point-kernel approximation for the count-rate estimation, N_{source}, resulted in notable deviations only at source-detector distance smaller than the distance travelled during one acquisition time interval.

Although the developed Bayesian algorithm used in this study was designed to estimate the position and activity of a single gamma-ray point source in two spatial dimensions, the approach can potentially be applied for multiple three-dimensional sources as long as there is sufficient spatial resolution in the measuring positions. Possibly, it may be developed to map spatial variability of the surface deposition of radionuclides in radiological emergency situations.

From the investigations of the developed Bayesian algorithm for car-borne orphan source search in papers I-III, it is possible to conclude that Bayesian methods are beneficial for estimation of position and activity of a single gamma-ray source in orphan source search applications in mobile gamma spectrometry.

Paper IV. Maximum detection distances for gamma emitting point sources in mobile gamma spectrometry

While deviating from the Bayesian methodology, the fourth manuscript is significant for the field of mobile gamma spectrometry, as it delves into the depths of the physics behind source detection during mobile measurements. At the heart of the fourth paper there is a maximal detection distance (MDD) algorithm, which calculates the *MDD* for gamma-ray point source of set activity, positioned some distance from the trajectory of the detector, while the detector passes the source in a straight line at a set speed. It depends on a number of parameters such as detector efficiency, vehicle speed, measuring time interval, natural radiation background level, accepted frequency of false alarms, etc. The algorithm was validated using experimental data from the AUTOMORC experiment described in section "AUTOMORC experiment set-up – Papers II-IV".

The results showed that by using the MDD algorithm it is possible to calculate the most advantageous combinations of vehicle speed, measurement time interval length (pulse acquisition time) and other search parameters for a range of source activities between 50 MBq and 1.2 GBq. Since the algorithm is based on physical laws for radiation transport, there is reason to believe that the MDD algorithm also describes maximum detection distances correctly for radiation sources up to at least TBq level, assuming a linear detector response. The MDD algorithm in its current form is based on fluences from an unshielded gamma source. If a radiation source

is shielded, its activity from the detector point of view becomes apparently lower. The calculations then apply to this lower apparent activity.

In order to achieve the longest possible detection distance to identify a photon source with a certain activity by mobile measurement, the best combination of measurement time interval and vehicle speed must be selected. This combination is independent of the detector type and efficiency. It depends on how the photon fluence is distributed along the vehicle's path past the source and therefore on the source's activity. The MDD algorithm gives for example at hand that at a vehicle speed of 50 km/h, the most advantageous measuring time interval is 5 seconds when searching for unshielded sources with activity in the order of 100 MBq. To detect higher activity sources at the same speed, longer measurement time intervals (10-20 seconds) are better. However, if the speed of the vehicle is increased, shorter time intervals should be selected. At the same time the maximum detection distance will be reduced. MDD values for 2 × 4l NaI(Tl) detector using different lengths of acquisition interval passing a ^{137}Cs source at 50 km/h is displayed in Fig. 34.

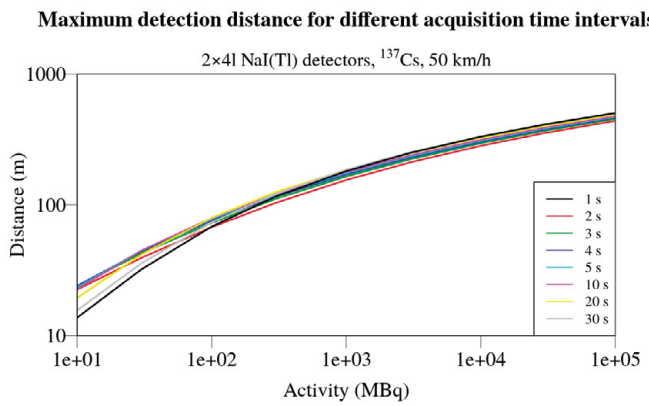

Fig. 34. Maximum detection distance for different acquisition time intervals for 4 litre NaI(Tl) detector. Figure from paper IV.

Summing the results of the fourth manuscript, it is evident that there are many parameters which influence the MDD, such as detector efficiency, vehicle speed, measuring time interval length, natural radiation background level, accepted frequency of false alarms, etc. One of the most straightforward conclusions is that MDD is directly dependent on the counting efficiency of the detector – the higher the efficiency the larger the MDD. However, environments with high levels of background radiation will reduce the MDD regardless of the counting efficiency of the detector. For a particular detector system in a specific situation it is still possible to increase the MDD by choosing the best combination of the vehicle

speed and acquisition time interval, depending on the presumed activity of the source. If this information about the source is unknown beforehand, then the best strategy is to drive past the source at the lowest speed possible combined with the shortest acquisition time available. Then, the data should be after-processed, combining the acquisition time intervals in various ways to obtain the best MDD for the source.

Calculations using the MDD algorithm provides an understanding on how different parameter settings such as detection probability, false alarm rates, background level, vehicle speed, acquisition time intervals and source activities will influence the MDD in mobile search of lost sources. The MDD algorithm may thus be able to present the most favourable acquisition time interval for any combination of vehicle speed and source activity, thus aiding an emergency search team in choosing the best parameter set-up for a specific mission.

Paper V. Applicability of a Bayesian method for reconstruction of ground activity deposition based on synthetic airborne gamma spectrometric data

Reconstruction of radionuclide spatial distribution in the area was performed using data from a fictitious UAV-borne detector, with sensitivity only a scalar to the primary photon flux in the voxels, for several altitudes of the detector – h=6, 10 and 15 m. Fluence of 662 keV primary photons, and reconstructed surface deposition densities of ^{137}Cs were compared for each altitude in Figs. 35-37. It can be seen that the quality of the reconstructed activity distribution is severely affected by the altitude of the detector. The higher the detector altitude, the lower the quality (in terms of spatial resolution and agreement with simulated true values) of the reconstruction. This is expected, because the angular distribution of the primary photons changes, which reduces the resolution of the data [37]. At altitude h=6 m, the resolution of the reconstruction is the best, and the pattern of the street around the neighbourhood can be identified.

Mean values of reconstructed spatial activity throughout the areas were calculated for each altitude of the detector (h = 6, 10 and 15) and cleanup scenario 0-3. Ratios of calculated mean spatial activity values were calculated by dividing the obtained mean spatial activity value for any cleanup scenario by the value for cleanup scenario 0 for all altitudes of the detector. Resulting table of average activity density ratio values is displayed in Table 4. This table displays the relative change in average spatial activity for a certain cleanup scenario. It can be seen, that cleanup scenarios 1-2 where either streets or the roofs or the streets were decontaminated, yielded in very similar reduction in average activity – 7-10 %. Decontamination of soil resulted in the biggest difference of about 58 %.

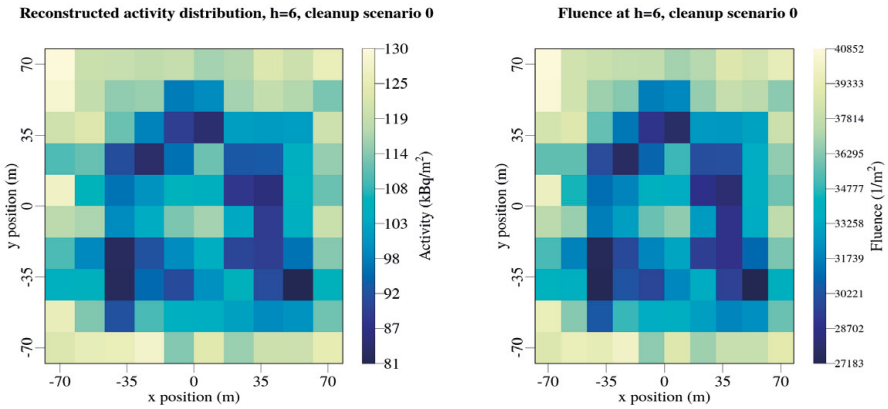

Fig. 35. Reconstructed spatial distribution of deposited activity per square metre in the area for altitude of the detector 6 m and cleanup scenario 0 (left). The fluence data used to obtain the reconstruction (right). The street and the houses are visible as low activity spots in reconstruction.

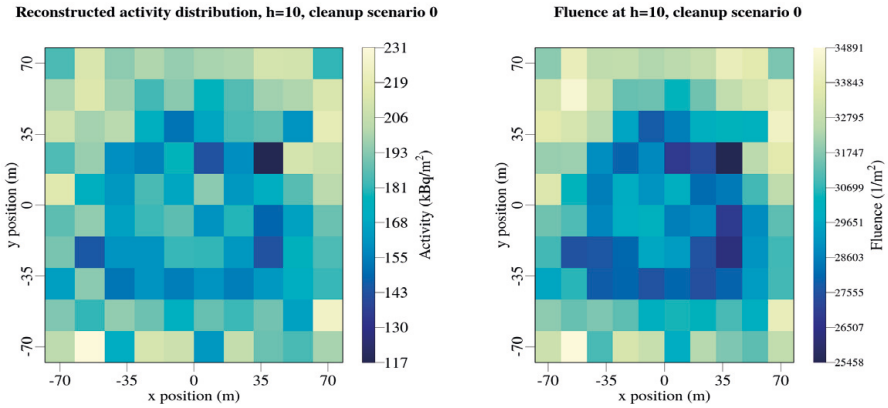

Fig. 36. Reconstructed spatial distribution of deposited activity per square metre in the area for altitude of the detector 10 m and cleanup scenario 0 (left). The fluence data used to obtain the reconstruction (right). The street can still be barely identified in the reconstruction.

Table. 4. Ratios of reconstructed spatial activity values.

Cleanup scenario	Ratio of mean activities throughout the area for detector altitude		
	h=6	*h*=10	*h*=15
0	1	1	1
1	0.9	0.9	0.9
2	0.93	0.93	0.93
3	0.42	0.41	0.42

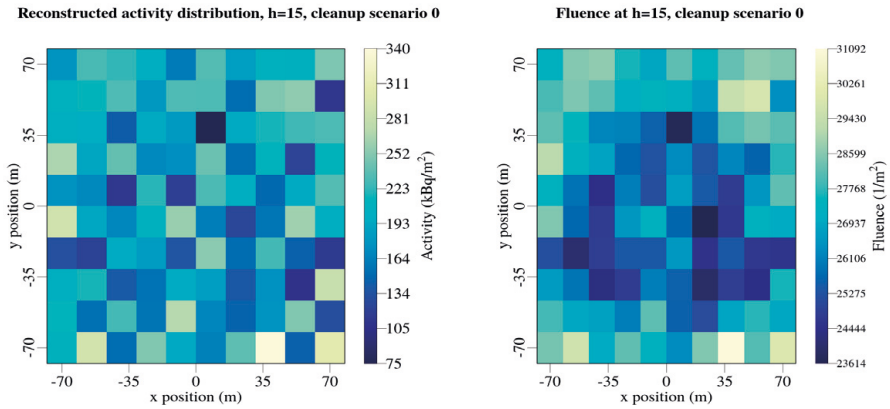

Fig. 37. Reconstructed spatial distribution of deposited activity per square metre in the area for altitude of the detector 15 m and cleanup scenario 0 (left). The fluence data used to obtain the reconstruction (right). Neither houses nor the street can be identified in the reconstruction.

The results indicate that spatial distribution of radionuclides can be estimated using Bayesian methods, despite the fact that the spatial resolution of the reconstructions is only 14 m, which is greater than the altitude of the detector for the two smaller values of (h = 6 and 10 m). The resolution was set so low due to the computational limitations of the relatively simple Metropolis-Hastings algorithm utilised.

When the number of dimensions in the posterior distribution increase significantly, efficient computation methods are needed. Even for a 10 × 10 surface deposition point matrix the algorithm has to evaluate activities of 10^2 points. Furthermore, the inside detector response matrix, R_{inside}, described in Eq. 31, can start to take up significant memory size for a larger number of surface deposition and measurement points. For 23 × 23 surface deposition points and 23 × 23 measurement points, the size of this response matrix is 1.3 MB. Increasing the size of both matrices to 113 × 113 yields a response matrix of 1.4 GB. For such resolution the algorithm would need to solve activities for 113^2=12769 surface deposition points. Some computational "short-cuts" like sparse matrices or other MCMC methods, like Hamiltonian Monte-Carlo might be the solution. That is out of the scope of this feasibility test but important for future investigation and method optimization.

General discussion

Why Bayesian?

There are many approaches to solving source localization and radionuclide spatial distribution estimation problems discussed in this thesis. One of such approaches could be likelihood function optimization to obtain values of parameters yielding the highest probability [57], [58]. In terms of finding the most probable solution – the Bayesian approach and optimization methods should technically obtain the same values of parameters of interest. For more complicated, multidimensional problems, like discussed in paper V, it might be even easier to utilise the optimization technique, as suggested by Zhang et al. [59]. Despite that, the most significant difference between the methods is that function optimization finds the value of the parameter(-s) of interest with the highest probability, and MCMC in Bayesian methods integrates the posterior distribution. Taking an example where optimisation and MCMC are used for estimating the activity of a radioactive source the optimization will yield only one value of activity (that is, the activity value with the highest probability). In contrast, MCMC will provide the probability distribution of this activity. Depending on the parameters of MCMC algorithm, the resulting posterior distribution should tell the uncertainty of the activity value given the model and the data. Although, MCMC is more computationally intensive, evaluated uncertainties of the parameters of interest in mobile gamma spectrometry may provide the decision-makers in emergency situations with more helpful information than using single values.

Due to advancements in computational resources, it is now possible to run parallel tasks efficiently in computers. Despite that, it is hard to directly employ efficient parallelization within one MCMC chain due to the dependence of the new proposed sample on the previous sample. However, it is possible to run multiple MCMC chains simultaneously with different initial starting parameters and random seeds. This would result in an increased number of obtained posterior samples per computation time, and thus more accurate posterior distributions. Despite the increased number of parallel chains, the number of MCMC iterations needed for any given chain to reach the target distribution will probably not change much if the MCMC algorithm is well-tuned.

Applicability of Bayesian methods to mobile gamma spectrometry data: the importance of data quality

The broad applicability of Bayesian and MCMC methods is well known [42], [45], [60], and it is no surprise that this versatility is reflected in the results of this thesis. Investigations of the applicability of Bayesian methods in mobile gamma spectrometry covered in papers I-III (carborne systems for orphan source search) and V (UAV-borne systems for the spatial distribution of ground deposition), in an area of interest, show that it is possible to utilise the Bayesian approach in mobile gamma spectrometry data. However, it has to be stressed that the accuracy of a particular Bayesian model is heavily dependent on the quantity of spatial data and on the quality of the sampled data, as the Bayesian theorem inherently implies that more data collection (information) will result in better quality predicted values in terms of estimated posterior distribution of parameter values.

Despite the effort put in to increasing the quality of the data and decrease the influence of e.g. background radiation [25], [61]–[65], or uncertainties in the geographical coordinates of the measurements perturbing the data [66], the reality is that there will always be some uncertainties in measurements performed with equipment. Some of these uncertainties can be taken into account while performing the data analysis, while some others are inherently governed by randomness. One of such random uncertainties is displayed in Fig. 23, when the clock controlling the time-tagging of sampled gamma spectra and geographical coordinate read-out is not stable enough, leading to erroneous geographical coordinates for single measurement points that varies during the collection of data-series. Because both of the developed algorithms are statistical data analysis methods primarily, such uncertainties can have significant effect on the uncertainties in the estimations. This is visible by comparing Fig. 23 with Fig. 32 and Fig. 33, where relative deviations of position and activity for estimations obtained using data from all detectors are visualised as a function of SNR. It can be seen, that the uncertainties for theoretical data (Fig. 23) is significantly smaller compared to the experimental data (Fig. 32 and Fig. 33).

Stemming from the evaluation of angular variations in counting efficiency of the detectors in paper II, one of the essential improvements is ensuring that the detectors are mounted in the vehicle so that the shielding in the plane of interest around the detector is such that the efficiency variations are as slight as possible, trying to avoiding dead spots as can be seen in Fig. 21 for the HPGe detector. Probably, it would be best to position the HPGe detector vertically above the roof, to obtain the most uniform efficiency for all angles of incidence in the plane of vehicle movement. For NaI(Tl) detectors, it could be argued that the best arrangement would be to position the two detectors vertically on the opposite sides of the vehicle, so that they would shield each other from the photons coming from the opposite side of the vehicle. In this way it would be possible to determine

which side of the road/vehicle trajectory the photons are coming from, while minimising the angular variations in the counting efficiency (illustrated in Fig. 21).

The uncertainties pertaining to the estimation of geographical coordinates of the measurements should be approached similarly. In principle, if the resolution of the obtained geographical coordinates is worse than the detector sampling interval (14 m throughout the papers I-III), the uncertainty in the data and subsequently in the Bayesian predictions, will therefore increase. In a particular case of the measurement vehicle used throughout the thesis (described in Fig. 19) with Nugget system and 123 % HPGe and 2x4 l NaI(Tl) detectors, the uncertainties manifested themselves in random coordinate shifts along the trajectory of the vehicle. These deviations can potentially affect the localization of the source along the road, and even reduce the estimated activity, as displayed in paper III. To alleviate these particular uncertainties several things can be done: i) reading of the geographical coordinates produced by the GNSS receiver using a different clock than the main program sequence and then correct the time-tagging afterwards, ii) setting the clock of the GNSS receiver as the main clock controlling the measurement interval which would require much change in the software iii) utilization dual frequency GNSS units, and/or iv) implementation of an inertial navigation system [67]–[69] to accurately calculate the position, velocity and attitude of the vehicle at any given moment.

Furthermore, the same argument can be made for the selection of the acquisition time interval. Theoretically, any finite length of acquisition time interval results in a loss of spatial data (merging of events into a single time-interval), thus using list-mode operation of detection equipment would offer the most detailed information about the radiation field [70], [71]. Using the gamma spectrometry equipment in this mode would increase the computational resources significantly (especially in areas of higher activity), due to individual registration of each photon.

Comparison of source detection rates using Bayesian methods with alarm threshold levels

At this point it becomes very interesting to compare the two methodologies discussed throughout the thesis in terms of source detection rates. Detection probabilities using Bayesian and alarm threshold methodologies for the AUTOMORC experiment data from set-ups 16 and 20 for ^{137}Cs and ^{60}Co sources were compared. Both methods were using combined data from two 4l NaI(Tl) spectrometers in the vehicle.

The MDD values predicted using the MDD algorithm developed in paper IV are within good agreement with the experimental data. For set-ups 16 and 20, the experimental probabilities of detecting the ^{137}Cs and ^{60}Co sources are displayed in

Table 5. Alongside, the calculated MDD values for 50 % probability of detection for the same source activity, vehicle speed and acquisition interval length are also displayed in Table 5. It can be seen, that for both set-ups the distance from the source to the road was higher than the MDD value for 50 % probability, which is is in agreement with the experimental source detection probabilities $P_{\text{experimental}}$.

Table. 5. Comparison of detection probabilities for alarm threshold ($P_{\text{experimental}}$) and Bayesian (P_{bayes}) methods. The calculated MDD distance is the average of the calculated left and right MDD (the right distance is longer than the left by about 5 m) for 50% probability of detection. The probability observed for source detection in the experiment is the average for sources to the left and the right.

Set-up number	Source	Activity (MBq)	Distance (m)	MDD for activity $P_{50\%}$ (m)	$P_{\text{experimental}}$ (%)	P_{Bayes} (%)
16	^{137}Cs	802	164	132	25	100
	^{60}Co	583	164	128	17	100
20	^{137}Cs	1215	164	151	84	100
	^{60}Co	1119	194	161	0	100

For the same experimental data from set-ups 16 and 20 Bayesian estimations were made using data from 2x4l NaI(Tl) detectors only. If the algorithm provided a clear indication that there is a source, it was regarded as a detection of the source despite the discrepancy between the estimated and actual values of source activity and position, displayed in Table 6. Due to the low SNR of the data for these experimental set-ups, the estimated positions and activities of the sources were not accurate. Maximum value of calculated relative deviation of estimated position were not greater than 0.77 throughout all of the results. This indicates that the estimated position of the source was within about 80% of the position of the source in terms of the distance from the source to the road (Table 6).

Table. 6. Relative deviations of estimated positions in terms of distance from the source to the road side for every pass of the sources in experimental set-ups 16 and 20. It can be seen, that the maximum value of relative deviation of position is lower than 1, indicating that although the estimated position of the source was not accurate, the source was detected.

Set-up number	Source	Relative deviation of estimated position							Maximum value
16	^{137}Cs	0.16	0.07	0.47	0.35	0.07	0.07	0.65	0.65
	^{60}Co	0.38	0.22	0.07	0.46	0.16	0.77	0.21	0.77
20	^{137}Cs	0.67	0.29	0.29	0.21	0.25	0.07	0.47	0.67
	^{60}Co	0.37	0.44	0.43	0.38	0.57	0.32	0.07	0.57

Furthermore, the Bayesian algorithm correctly found the peak in the measurement time-series for every single estimation (illustrated in Fig. 38).

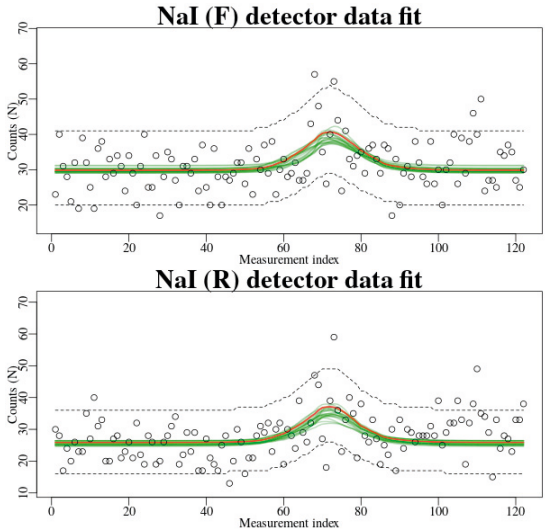

Fig. 38. Measurement time-series data for both of the NaI(Tl) detectors (front – top, rear – bottom) is displayed by black circles while passing a ^{60}Co source in set-up 20. Calculated count-rate function for the measurement positions given the actual source position and activity is displayed with a red line, which is slightly different for the two detectors due to the different angular variations in counting efficiency. Green lines represents predictions of the Bayesian algorithm throughout the MCMC iterations.

This leads to 100 % detection rate P_{Bayes} for all of the sources and set-ups, as displayed in Table 5. The explanation why the Bayesian method is better than the alarm method, is that when the alarm threshold is set so high for one-second acquisition intervals to have only one false alarm per 1 hour, then only one (best alignment) or two (worst alignment) one-second acquisition intervals will in practice produce an alarm when the source is at or beyond the MDD. If acquisition time intervals of 10 - 20 seconds had been used instead, with a speed of 50 km/h and with source activities ranging between 100 - 1000 MBq, the MDD would increase by about 20% for ^{137}Cs and 25% for ^{60}Co. The Bayesian method can directly use more acquisition intervals for an extensive range of source activities with counts below the alarm level without choosing an optimal acquisition time interval.

If such Bayesian method would be implemented in a way, that estimations of source position and activity could be obtained in real time, it would be possible to utilize the lower detection limit in orphan source search missions to extend the MDD of the system. Then, when the Bayesian algorithm provides a rough real time solution of the position and activity of the source, either another mobile pass of the source or some additional stationary measurements could be performed to collect more data and to obtain more accurate source and activity estimations. To visualise this, posterior distributions for position and activity of a ^{137}Cs source were evaluated for two situations using simulated data:

1. A single pass of the source performed at a 50 km/h with 1 s acquisition time using the two 4l NaI(Tl) detectors;
2. A single pass of the source as described above, with additional 3 stationary measurements of 30 seconds performed at the point with closest source-detector distance and two additional points, with source-detector distance set to around 1.5 the smallest source-detector distance.

The distance to the source was set to 100 m and activity of the source – 150 MBq, so that it was barely noticeable in the synthetic measurement time-series for the detectors, as illustrated in Fig. 39. After running the Bayesian algorithm for 30 000 iterations, the obtained posterior distributions for the first situation are displayed in Fig. 40. It is evident, that the uncertainty in the posterior distributions is very high, and the discrepancy between the actual position and activity of the source is significant. For the second situation, the results are relatively different, as displayed by Fig. 41. It can easily be seen, that the uncertainty in the posterior distributions is greatly reduced by adding only 1.5 minutes worth of data.

Such methodology in orphan source detection could increase the maximal distance at which sources could be detected at the same time providing with estimated position and activity of the source. Given that enough data is collected, the accuracy of the estimations might be such, that additional survey using hand-held equipment might be not needed.

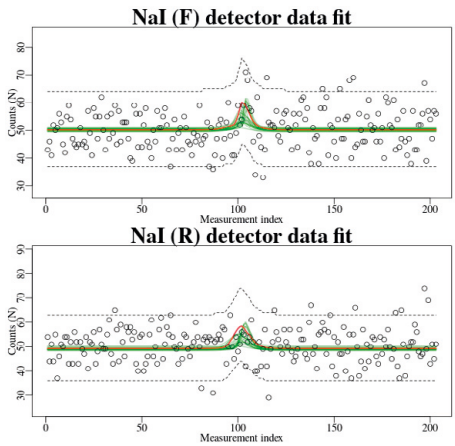

Fig. 39. The resulting simulated count-rate time-series for the two 4l NaI(Tl) detectors. Calculated count-rate function for the measurement positions given the actual source position and activity is displayed with a red line. Green lines represents predictions of the Bayesian algorithm throughout the MCMC iterations.

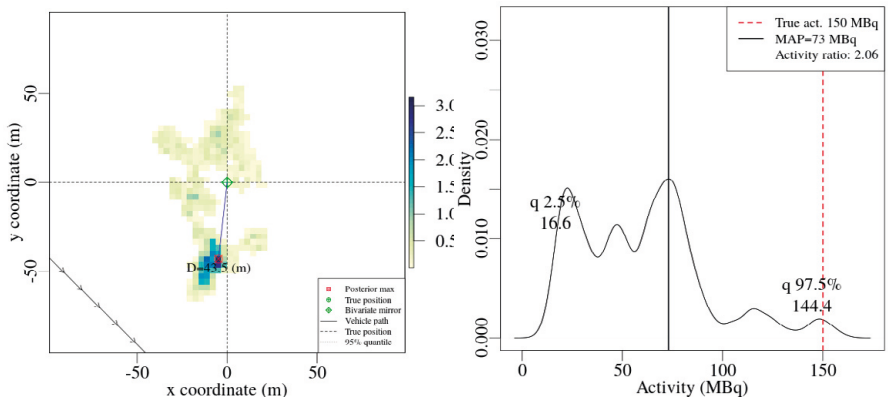

Fig. 40. Posterior distributions for source position (left) and activity (right) using only the data from a single pass of the source. The distance between the actual position of the source marked by a cross of dashed lines to the position of maximum probability is displayed by D in the graph. For this estimation, the distance is 43.5 m. The estimated activity was 73 MBq, while the actual activity was 150 MBq.

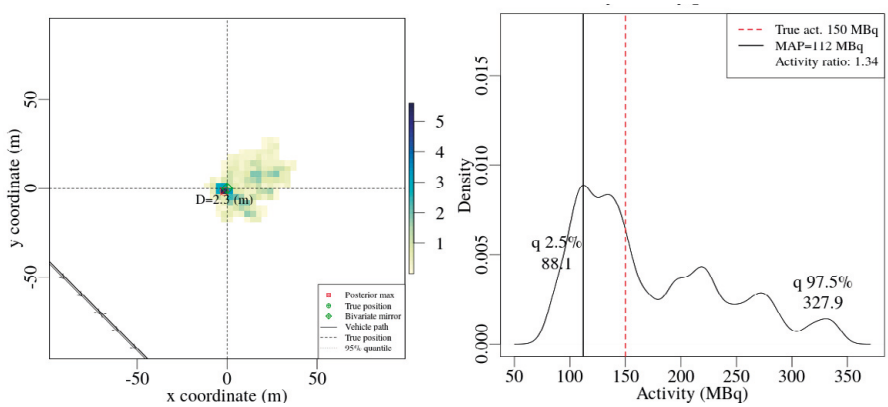

Fig. 41. Posterior distributions for source position (left) and activity (right) obtained using the additional data with the data obtained during the pass. The distance between the actual position of the source marked by a cross of dashed lines to the position of maximum probability is displayed by *D* in the graph. For this estimation, the distance is 2.3 m. The estimated activity was 112 MBq, while the actual activity was 150 MBq.

Outlook and limitations

The work discussed in this thesis barely scratches the surface of the use of Bayesian applications in mobile gamma spectrometry, only showcasing its potential use in the field. The developed Bayesian algorithm is still very fundamental and requires a significant amount of knowledge in Bayesian methods

and programming skills to use at this point. The whole data reading, preparation, inference and plotting algorithm developed throughout the thesis is made up of R scripts, totalling to thousands of lines of code, which require hands-on programming to alter/modify the behaviour of the algorithm. The most advanced version of the orphan source algorithm can currently solve the localisation and activity for multiple gamma-ray point sources (tested for 3 sources using experimental data). The algorithm designed to map the spatial distribution of the radionuclides in the area from UAV-borne measurements is currently limited to 20×20 surface deposition point and measurement grids due to computational limitations, which is sufficient for a proof-of-concept study. Source code of the algorithms is available on GitHub [72], [73].

These algorithms can be developed further, by introducing a graphical user interface which will allow people with less technical prowess to utilise the power of Bayesian methods for mobile gamma spectrometry data. Additionally, a methodology for detector data read-out might be considered, to develop and test the applicability of these methods in real-time.

Further studies might combine LIDAR technology, UAV-borne gamma spectrometry and Bayesian methods for highly accurate estimations of spatial distribution of deposited radionuclide in a three-dimensional space, which could be large-scale fallout areas with vegetations (shrubberies and trees) and houses, or on building structures in nuclear energy facilities. Additionally, it would be interesting to test how to combine mobile gamma spectrometric data from car-borne and UAV-borne measurements and measurements on foot to obtain a more comprehensive and accurate estimation of the spatial distribution of gamma emitters on contaminated surfaces and structures.

Conclusions

In this thesis, the applicability of Bayesian statistical methods to analyse mobile radiometry data in radiological emergencies has been investigated, as a prospective toolset to obtain additional information for decision-makers in emergency situations, which may be understaffed, and may sometimes lack time and sensitive equipment. As a result, two Bayesian algorithms were subsequently developed, one for orphan source search and the other for estimation of the spatial distribution of radionuclides within an area using gamma spectrometric data obtained by a fictitious unmanned aerial vehicle borne detector. It can be concluded, that:

- Bayesian methods can be successfully applied to mobile spectrometry data, yielding additional information for the decision makers in radiological emergency situations.
- The developed algorithm for orphan source search could be utilised in its current form for real emergency situations.
- Application of Bayesian methods in orphan source search can probably offer better detection probability as the method utilises all of the data. However, further investigations are needed to demonstrate this.
- The algorithm for mapping the spatial distribution of a radionuclide surface deposition in an area can be used as it is, if rough estimates of the radionuclide distribution are needed. If significant spatial resolution over larger areas (>10,000 m^2) is required, the algorithm must be developed further.
- Because Bayesian methods is a statistical data analysis method, the quality of the data is crucial, and will be the determining factor in the accuracy of the estimates. All of the factors discussed throughout the thesis; signal-to-noise ratio of the data, angular variations of counting efficiency and uncertainties of geographical coordinate will have a cumulative effect on the estimations. Some of these factors, such as angular response of the detector, might be omitted with a respective calibration, while others, like signal-to-noise ratio of the data, should be maximised.

Acknowledgements

First and foremost I would like to say a sincere and immensely big – thank you – to all of my supervisors:

Christopher Rääf
Thank you for believing in me and providing me with the opportunity to learn a lot not only about the radiation physics and writing scientific articles but also about myself. Thank you for your immense patience, methodical teaching and attention to the details – indeed, as you have said to me many times – the devil is in the details!

Robert Finck
Thank you for your patience while listening to my ideas and for your time discussing the most intricate little details about things. You always had time for discussions!

Jonas Wallin
Thank you for opening the doors to the Bayesian world!

Mattias, thank you for the endless chats and coffees that we had! Either by the table or somewhere outside of Gävle, in highly radioactive forests…

Peder, Simon and others from SSM for making this thesis and all of the awesome included experiences (NEDFALL, HAVSÖRN, etc.) possible.

All of the colleagues in the Medical Radiation Physics department in Malmö:

LEO, Christian, Lovisa, Sven, Magnus, Guillaume, Sören, Viveca, Emma, Daniel, Hannie, Gustav, Irma, Johan, Anders, Lena, Pernilla, and all of the others!

If for any circumstance I have forgotten someone, please, do not hesitate and write your name here: _____

Undoubtedly, to all of my family for strength, support and inspiration...

And all of the stars in the Universe for arranging themselves to make this possible!

This PhD study was funded by a grant from the Swedish Radiation Safety Authority.

References

[1] IAEA, “Environmental Consequences of the Chernobyl Accident and their Remediation: Twenty Years of Experience,” 2006.

[2] IAEA, “The Fukushima Daiichi Accident Report by the Director General,” 2015.

[3] L. Cui, Y. Taira, M. Matsuo, M. Orita, Y. Yamada, and N. Takamura, “Environmental Remediation of the difficult-to-return zone in Tomioka Town, Fukushima Prefecture,” *Sci. Rep.*, vol. 10, no. 1, pp. 1–8, 2020.

[4] IAEA, “Radiation Protection and Safety of Radiation Sources: International Basic Safety Standards General Safety Requirements Part 3,” International Atomic Energy Agency, 2014.

[5] IAEA, “The radiological accident in Lia, Georgia,” 2014.

[6] IAEA, “The radiological accident in Goiânia. Volume 815 de Proceedings series,” 1988.

[7] H. W. Taylor, E. A. Hutchison, K. L. Mcinnes, and J. Svoboda, “Cosmos 954: Search for airborne radioactivity on lichens in the crash area, Northwest territories, Canada,” *Science (80-.).*, vol. 205, no. 4413, pp. 1383–1385, 1979.

[8] L. J. Deal, J. F. Doyle, Z. G. Burson, and P. K. Boyns, “Locating the lost athena missile in mexico by the aerial radiological measuring system (ARMS),” *Health Phys.*, vol. 23, no. 1, pp. 95–98, 1972.

[9] B. L. Tracy, F. A. Prantl, and J. M. Quinn, “Health impact of radioactive debris from the satellite Cosmos 954,” *Health Phys.*, vol. 47, no. 2, pp. 225–233, 1984.

[10] UNSCEAR, *Sources and Effects of Ionizing Radiation*, vol. II. United Nations Scientific Committee on the Effects of Atomic Radiation, 2010.

[11] T. Hjerpe, R. R. Finck, and C. Samuelsson, “STATISTICAL DATA EVALUATION IN MOBILE GAMMA SPECTROMETRY: AN OPTIMIZATION

OF ON-LINE SEARCH STRATEGIES IN THE SCENARIO OF LOST POINT SOURCES," *Health Phys.*, vol. 80, no. 6, pp. 563–570, 2001.

[12] J. Kim, K. T. Lim, K. Ko, E. Ko, and G. Cho, "Radioisotope Identification and Nonintrusive Depth Estimation of Localized Low-Level Radioactive Contaminants Using Bayesian Inference," *Sensors*, 2019.

[13] B. Ristic and A. Gunatilaka, "Information driven localisation of a radiological point source," *Inf. Fusion*, vol. 9, no. 2, pp. 317–326, 2008.

[14] B. Ristic, M. Morelande, and A. Gunatilaka, "Information driven search for point sources of gamma radiation," *Signal Processing*, vol. 90, no. 4, pp. 1225–1239, 2010.

[15] R. A. Cortez *et al.*, "Smart radiation sensor management," *IEEE Robot. Autom. Mag.*, vol. 15, no. 3, pp. 85–93, 2008.

[16] B. Ristic, M. Morelande, and A. Gunatilaka, "A controlled search for radioactive point sources," *Proc. 11th Int. Conf. Inf. Fusion, FUSION 2008*, 2008.

[17] M. R. Morelande and B. Ristic, "Radiological source detection and localisation using Bayesian techniques," *IEEE Trans. Signal Process.*, vol. 57, no. 11, pp. 4220–4231, 2009.

[18] A. Gelman, J. B. Carlin, H. S. Stern, D. B. Dunson, A. Vehtari, and D. B. Rubin, *Bayesian Data Analysis*, 3rd ed. Taylor & Francis Ltd, 2013.

[19] National Institute of Standards and Technology, "X-Ray Mass Attenuation Coefficients," 2004.

[20] T. Hjerpe, R. R. Finck, and C. Samuelsson, "Statistical data evaluation in mobile gamma spectrometry: An optimization of on-line search strategies in the scenario of lost point sources," *Health Phys.*, vol. 80, no. 6, pp. 563–570, 2001.

[21] E. Prieto, E. Jabaloyas, R. Casanovas, C. Rovira, and M. Salvadó, "Set up of a gamma spectrometry mobile unit equipped with LaBr3(Ce) detectors for radioactivity monitoring," *Radiat. Phys. Chem.*, vol. 168, no. November 2019, p. 108600, 2020.

[22] S. Gutierrez, L. Guillot, and C. Bourgeois, "Contribution of a germanium detector in mobile gamma-ray spectrometry. Spectral analysis and performance," *Nucl. Instruments Methods Phys. Res. A*, vol. 482, no. 1–3, pp. 425–433, 2002.

[23] H. K. Aage and U. Korsbech, "Search for lost or orphan radioactive sources based on NaI gamma spectrometry," *Appl. Radiat. Isot.*, vol. 58, pp. 103–113, 2003.

[24] S. Long and L. Martin, “Optimisation of systems to locate discrete gamma-ray sources within a large search area,” *J. Environ. Radioact.*, vol. 94, no. 1, pp. 41–53, 2007.

[25] P. Kock, R. R. Finck, J. M. C. Nilsson, K. Östlund, and C. Samuelsson, “A deviation display method for visualising data in mobile gamma-ray spectrometry,” *Appl. Radiat. Isot.*, vol. 68, no. 9, pp. 1832–1838, 2010.

[26] T. Hjerpe and C. Samuelsson, “A COMPARISON BETWEEN GROSS AND NET COUNT METHODS WHEN SEARCHING FOR ORPHAN RADIOACTIVE SOURCES,” *Health Phys.*, vol. 84, no. 2, 2003.

[27] M. Isaksson and C. L. Rääf, *Environmental Radioactivity and Emergency Preparedness*, 1st ed. CRC Press, Taylor & Francis Group, 2016.

[28] M. Holmberg, K. Edvarson, and R. Finck, “Radiation doses in Sweden resulting from the Chernobyl fallout: A review,” *Int. J. Radiat. Biol.*, vol. 54, no. 2, pp. 151–166, 1988.

[29] P. G. Martin, O. D. Payton, J. S. Fardoulis, D. A. Richards, and T. B. Scott, “The use of unmanned aerial systems for the mapping of legacy uranium mines,” *J. Environ. Radioact.*, vol. 143, 2015.

[30] A. Parshin, V. Morozov, N. Snegirev, E. Valkova, and F. Shikalenko, “Advantages of gamma-radiometric and spectrometric low-altitude geophysical surveys by unmanned aerial systems with small scintillation detectors,” *Appl. Sci.*, vol. 11, no. 5, pp. 1–25, 2021.

[31] A. Vale, R. Ventura, and P. Carvalho, “Application of unmanned aerial vehicles for radiological inspection,” *Fusion Eng. Des.*, vol. 124, pp. 492–495, 2017.

[32] O. Šálek, M. Matolín, and L. Gryc, “Mapping of radiation anomalies using UAV mini-airborne gamma-ray spectrometry,” *J. Environ. Radioact.*, vol. 182, no. November 2017, pp. 101–107, 2018.

[33] D. T. Connor *et al.*, “Radiological comparison of a FDNPP waste storage site during and after construction,” *Environ. Pollut.*, vol. 243, pp. 582–590, 2018.

[34] P. Kock, C. Rääf, and C. Samuelsson, “On background radiation gradients - the use of airborne surveys when searching for orphan sources using mobile gamma-ray spectrometry,” *J. Environ. Radioact.*, vol. 128, pp. 84–90, 2014.

[35] S. Briechle, A. Sizov, O. Tretyak, V. Antropov, N. Molitor, and P. Krzystek, “UAV-based detection of unknown radioactive biomass deposits in Chernobyl’s

exclusion zone," *Int. Arch. Photogramm. Remote Sens. Spat. Inf. Sci. - ISPRS Arch.*, vol. 42, no. 2, pp. 163–169, 2018.

[36] L. Wallace, A. Lucieer, C. Watson, and D. Turner, "Development of a UAV-LiDAR system with application to forest inventory," *Remote Sens.*, vol. 4, no. 6, pp. 1519–1543, 2012.

[37] R. Finck, "High Resolution Field Gamma Spectrometry and its Applications to Problems in Environmental Radiology," Lund University, 1992.

[38] S. Almgren and M. Isaksson, "Vertical migration studies of 137Cs from nuclear weapons fallout and the Chernobyl accident," *J. Environ. Radioact.*, vol. 91, no. 1–2, pp. 90–102, 2006.

[39] C. P. Robert and G. Casella, *Monte Carlo Statistical Methods*. Springer, 2004.

[40] R Core Team, "R: A Language and Environment for Statistical Computing," Vienna, Austria, 2020.

[41] M. B. Lykkegaard, T. J. Dodwell, and D. Moxey, "Accelerating uncertainty quantification of groundwater flow modelling using a deep neural network proxy," *Comput. Methods Appl. Mech. Eng.*, vol. 383, p. 113895, 2021.

[42] Y. K. Ying, J. R. Maddison, and J. Vanneste, "Bayesian inference of ocean diffusivity from Lagrangian trajectory data," *Ocean Model.*, vol. 140, p. 101401, 2019.

[43] R. Sachak-Patwa, H. M. Byrne, and R. N. Thompson, "Accounting for cross-immunity can improve forecast accuracy during influenza epidemics," *Epidemics*, vol. 34, no. July 2020, p. 100432, 2021.

[44] H. Wu, Y. Chen, S. Li, and Z. Peng, "Acoustic impedance inversion using Gaussian metropolis–Hastings sampling with data driving," *Energies*, vol. 12, no. 14, pp. 1–15, 2019.

[45] J. T. Fischer, A. Kofler, A. Huber, W. Fellin, M. Mergili, and M. Oberguggenberger, "Bayesian inference in snow avalanche simulation with r.Avaflow," *Geosci.*, vol. 10, no. 5, pp. 1–17, 2020.

[46] H. Tran and K. Khoshelham, "Procedural reconstruction of 3D indoor models from lidar data using reversible jump Markov Chain Monte Carlo," *Remote Sens.*, vol. 12, no. 5, 2020.

[47] Q. Yang, E. B. Pitman, M. Bursik, and S. F. Jenkins, "Tephra deposit inversion by coupling Tephra2 with the Metropolis-Hastings algorithm: algorithm introduction

and demonstration with synthetic datasets," *J. Appl. Volcanol.*, vol. 10, no. 1, pp. 1–24, 2021.

[48] L. Zhang *et al.*, "Efficient reliability assessment method for bridges based on Markov Chain Monte Carlo (MCMC) with Metropolis-Hasting Algorithm (MHA)," *IOP Conf. Ser. Earth Environ. Sci.*, vol. 580, no. 1, 2020.

[49] M. Betancourt, "A Conceptual Introduction to Hamiltonian Monte Carlo," 2017.

[50] G. O. Roberts, A. Gelman, and W. R. Gilks, "Weak convergence and optimal scaling of random walk Metropolis algorithms," *Ann. Appl. Probab.*, vol. 7, no. 1, pp. 110–120, 1997.

[51] A. E. Gelfand and S. K. Sahu, "On markov chain monte carlo acceleration," *J. Comput. Graph. Stat.*, vol. 3, no. 3, pp. 261–276, 1994.

[52] C. Andrieu and J. Thoms, "A tutorial on adaptive MCMC," *Stat. Comput.*, no. 18, pp. 343–373, 2008.

[53] O. Karlberg, "Manual och teknisk beskrivning av CEMIK-systemet och NuggetW. Internal document (in Swedish).," 2014.

[54] J. Lepp, "Serpent – a Continuous-energy Monte Carlo Reactor Physics Burnup Calculation Code," *Tech. Res. Cent. Finl.*, p. 157, 2011.

[55] W. Lindberg, "Monte-Carlo response for mobile gamma spectroscopy in fallout affected residential areas," Uppsala University, 2021.

[56] Y. Hinrichsen, R. Finck, J. Martinsson, and C. Rääf, "Maximizing avertable doses with a minimum amount of waste for remediation of land areas around typical single family houses after radioactive fallout based on Monte Carlo simulations," *Sci. Rep.*, vol. 11, no. 1, pp. 1–9, 2021.

[57] J. Nocedal and S. J. Wright, *Numerical optimization 2nd edition*. 2000.

[58] S. Degirmenci, "A General Framework of Large-Scale Convex Optimization Using Jensen Surrogates and Acceleration Techniques," *ProQuest Diss. Theses*, p. 264, 2016.

[59] S. Zhang, R. Liu, and T. Zhao, "Mapping radiation distribution on ground based on the measurement using an unmanned aerial vehicle," *J. Environ. Radioact.*, vol. 193–194, no. August, pp. 44–56, 2018.

[60] G. Cabal and J. Kluson, "Air Kerma Rate estimation by means of in-situ gamma spectrometry: A Bayesian approach," *Appl. Radiat. Isot.*, vol. 68, no. 4–5, pp. 804–806, 2010.

[61] E. Mauring and M. A. Smethurst, “Reducing noise in radiometric multi-channel data using noise-adjusted singular value decomposition (NASVD) and maximum noise fraction (MNF).,” 2005.

[62] A. J. Cresswell and D. C. W. Sanderson, “The use of difference spectra with a filtered rolling average background in mobile gamma spectrometry measurements,” *Nucl. Instruments Methods Phys. Res. A*, vol. 607, no. 3, pp. 685–694, 2009.

[63] A. J. Cresswell, D. C. W. Sanderson, and D. C. White, “Cs measurement uncertainties and detection limits for airborne gamma spectrometry (AGS) data analysed using a spectral windows method,” *Appl. Radiat. Isot.*, vol. 64, pp. 247–253, 2006.

[64] T. J. Aucott, M. S. Bandstra, V. Negut, J. C. Curtis, D. H. Chivers, and K. Vetter, “Effects of background on gamma-ray detection for mobile spectroscopy and imaging systems,” *IEEE Trans. Nucl. Sci.*, vol. 61, no. 2, pp. 985–991, 2014.

[65] R. D. Penny *et al.*, “Improved radiological/nuclear source localization in variable NORM background: An MLEM approach with segmentation data,” *Nucl. Instruments Methods Phys. Res. Sect. A Accel. Spectrometers, Detect. Assoc. Equip.*, vol. 784, pp. 319–325, 2015.

[66] M. Albéri *et al.*, “Accuracy of flight altitude measured with low-cost GNSS, radar and barometer sensors: Implications for airborne radiometric surveys,” *Sensors (Switzerland)*, vol. 17, no. 8, 2017.

[67] A. B. Chatfield, *Fundamentals Of High Accuracy Inertial Navigation*. 1997.

[68] A. Noureldin, T. B. Karamat, and J. Georgy, *Fundamentals of inertial navigation, satellite-based positioning and their integration*. 2013.

[69] J. Tang *et al.*, “LiDAR scan matching aided inertial navigation system in GNSS-denied environments,” *Sensors (Switzerland)*, vol. 15, no. 7, 2015.

[70] K. Peräjärvi, J. Keightley, J. Paepen, O. Tengblad, and H. Toivonen, “List-mode data acquisition based on digital electronics - State-of-the-art report,” 2014.

[71] J. Nilsson, “Development and Optimisation of Methods for Locating and Mapping Lost Radioactive Sources,” Lund University, 2016.

[72] A. Bukartas, “GitHub repository for OrphanSource algorithm,” 2021. [Online]. Available: https://github.com/SpontaneousFusion/OrphanSource.

[73] A. Bukartas, “GitHub repository for GroundContamination algorithm,” 2021. [Online]. Available: https://github.com/SpontaneousFusion/GroundContamination.